TITLE:

Mechanism and Structure-Guided Optimization of SLC1A1/EAAT3-Selective Inhibitors in Kidney Cancer

Authors: Pooneh Koochaki[1,*], Biao Qiu[2,4,*], Jesse A. Coker[3,*], Alexander Earsley[2], Nancy S. Wang[3], Todd Romigh[3], Christopher M. Goins,[3] Shaun R. Stauffer[3,#], Olga Boudker[2,4,#], and Abhishek A. Chakraborty[1,5,#]

[1]Department of Cancer Biology, Lerner Research Institute, Cleveland Clinic, Cleveland, OH 44195

[2]Department of Physiology & Biophysics, Weill Cornell Medicine, New York, NY 10021

[3]Center for Therapeutics Discovery, Cleveland Clinic, Cleveland, OH 44195

[4]Howard Hughes Medical Institute, Weill Cornell Medicine, New York, NY 10021

[5]Case Comprehensive Cancer Center, Cleveland, OH 44106

*equal contribution

[#]To whom correspondence should be addressed:

Shaun R. Stauffer (stauffs2@ccf.org)

Olga Boudker (olb2003@med.cornell.edu)

Abhishek A. Chakraborty (chakraa@ccf.org)

Summary (150 Words)

Renal Cell Carcinomas (RCCs) depend metabolically on the trimeric sodium-coupled aspartate and glutamate transporter, SLC1A1/EAAT3; however, pharmacologically targeting SLC1A1 is challenging. We determined a cryo-EM structure of human SLC1A1 bound to compound **3e**, a recently described SLC1A1-selective bicyclic imidazo[1,2-α]pyridine-3-amine (BIA) inhibitor. **3e** binds a membrane-embedded, allosteric pocket accessible only in the *apo* state, when SLC1A1 is unbound to substrate and sodium. Wedged between the trimerization domain and the substrate-binding transport domain, together with a cholesterol moiety from the lipid bilayer, **3e** likely prevents sodium and substrate binding, and blocks SLC1A1's elevator-like movements that are essential for transport. Mutations in this pocket abolish **3e** binding and counteract **3e**'s cytotoxicity in RCC cells, confirming on-target activity and explaining SLC1A1 selectivity. A structure-guided medicinal chemistry effort yielded two new, SLC1A1-selective BIA derivatives, PBJ1 and PBJ2, with enhanced cytotoxicity resulting from the inhibition of SLC1A1-dependent aspartate, glutamate, and cysteine metabolic pathways.

Keywords: SLC1A1, EAAT3, cryo-EM, drug-resistant mutants, RCC, thermal shift assays, in silico docking, cellular IC_{50}, medicinal chemistry, impedance assays, metabolic regulation.

Introduction

Solute carriers (SLCs) are increasingly recognized for their roles in human diseases, including cancers.[1] Their localization to the cell surface makes them accessible to pharmacological agents, rendering them inherently druggable and therapeutically valuable. Furthermore, compared to normal tissues, the aberrant metabolic demands of tumors heighten their reliance on SLC activity, creating a therapeutic window for selective cancer targeting.[2]

We previously identified SLC1A1 (also known as Excitatory Amino Acid Transporter 3, EAAT3) as an oncogenic dependency in clear cell Renal Cell Carcinomas (ccRCCs)[3] – the most common form of adult kidney cancer.[4] Others have reported SLC1A1 as a metabolic vulnerability in fibrosarcoma,[5] lung cancer,[6,7] hematologic malignancies,[8] and brain tumors.[9] SLC1A1 imports aspartate (L-Asp), glutamate (L-Glu), and, to a lesser extent, cysteine (L-Cys) from the extracellular space.[10-14] L-Asp is essential for cancer cell growth because it provides the carbon skeleton for nucleotide biosynthesis.[15] Moreover, L-Asp's poor cellular permeability and scarcity in hypoxic environments lead to an increased dependence on its transporters in solid tumors.[16,17] L-Glu supports reductive carboxylation in hypoxic tumors and, along with L-Cys, serves as a precursor for glutathione, aiding the oxidative stress response.[18-20]

The SLC1A1 paralog, SLC1A2 (EAAT2), is predominantly expressed in the central nervous system (CNS), where it constitutes 1-2% of total protein in the forebrain.[21,22] It is crucial for mammalian glutamate-mediated synaptic transmission and survival. In

contrast, although SLC1A1 is broadly expressed, homozygous loss of *Slc1a1* is well tolerated in mice. These mice show elevated urinary excretion of L-Asp and L-Glu (aminoaciduria); however, SLC1A1 loss does not cause neurodegeneration unless exposed to hypoxia or oxidative stress.[23-25] Similarly, SLC1A1 inactivation in humans results in aminoaciduria and minor cognitive symptoms, with minimal additional manifestations and normal life expectancy.[10] These observations suggest that global (and transient) SLC1A1 inhibition is likely safe in humans, supporting the development of selective inhibitors for cancer therapy.

All SLC1 transporters utilize an “elevator” mechanism for substrate uptake (**Figure 1A**).[26-32] These homotrimeric carriers consist of a central trimerization or scaffold domain and a peripheral transport domain, which moves across the membrane from the outward-facing (OF) to the inward-facing (IF) position. In the OF conformation, the transport domains bind the substrate and co-transported Na^+ from the extracellular space, then translocate to the IF conformation to release them into the cytoplasm. During the return to the OF state, they translocate a K^+ ion from the cytoplasm to the outside, completing the cycle.[13,29,31]

Most current SLC1 inhibitors are competitive L-Asp-derived compounds, such as DL-threo-β-benzyloxyaspartic acid (TBOA)[33] and its trifluoromethyl-benzoyl derivative (TFB-TBOA)[34], which lack selectivity and drug-like properties necessary for transition into the clinic. A recent study described a series of bicyclic imidazopyridine amine (BIA) SLC1 inhibitors, with compound **3e** emerging as the best-in-class SLC1A1-selective agent.[35]

Notably, **3e** shares no structural similarity with SLC1A1's canonical substrates, raising questions about its on-target engagement and mechanism of action. Moreover, although **3e** inhibits cancer cell growth *in vitro*, it exhibits poor solubility and low kidney bioavailability.[3] Lastly, **3e** contains an unsubstituted furan ring, making it vulnerable to hepatic clearance by the cytochrome P450 enzymes. Thus, **3e** is not suitable for *in vivo use* and offers limited clinical potential.

We report a cryogenic electron microscopy (cryo-EM) structure of human SLC1A1 bound to compound **3e**. Remarkably, **3e** occupies an allosteric pocket between the Na^+-binding site and the substrate-binding gate, accessible only in SLC1A1's *apo* state, unbound to Na^+ and substrate. The structure reveals the transporter in an IF *apo* state where **3e** and a cholesterol snuggle between the transport and scaffold domains. These findings suggest a novel inhibition mechanism in which **3e** prevents Na^+ and substrate binding and likely traps the transporter in the IF conformation. Functional analysis reveals that F99 and T402 in SLC1A1 are essential for **3e**-induced cytotoxicity, with the non-conserved F99 residue conferring selectivity towards SLC1A1. Structure-guided modifications of the BIA scaffold led to the identification of PBJ1 and PBJ2, two SLC1A1-selective inhibitors with improved cancer cell-killing potency. Genetic and metabolic rescue assays confirm that PBJ1 and PBJ2's cytotoxicity is on-target and stems from the depletion of key L-Asp-, L-Glu-, and L-Cys-derived metabolites. These findings reveal a previously unrecognized mechanism of SLC1 inhibition, providing a foundation for the development of SLC1A1-targeted therapies.

Results

Cryo-EM structure of SLC1A1/EAAT3 with Compound 3e

To assess **3e**'s mechanism of inhibition, we imaged recombinantly expressed human SLC1A1 with mutated glycosylation sites (SLC1A1g; see Methods) in the presence of 200 mM NaCl and 100 µM **3e** by cryo-EM. Particle alignment with imposed three-fold symmetry yielded an EM map at an overall resolution of 2.46 Å, revealing the transporter in an IF conformation (**Figures S1 and Supplementary Table 1**), similar to our previously reported structure.[30,31] Since each protomer in the trimer functions independently,[31,36-38] we applied symmetry expansion and protomer classification without alignment, revealing three major structural classes (**Figure S1 and Supplementary Table 1**). One class, resolved at 2.83 Å, pictured an IF protomer bound to Na^+ ions (**Figure 1B**), indistinguishable from the previously reported Na^+-bound SLC1A1g structure (**Figure S2A**). Two other classes (designated A and B), resolved at 2.56 and 2.76 Å, respectively, resembled the *apo* IF conformation of SLC1A1g determined in the absence of Na^+ ions and substrates (**Figures 1C-1E**). No density corresponding to **3e** was observed in the Na^+-bound protomers. In contrast, clear nonprotein density consistent with **3e** was present in both *apo* protomers (**Figures 1D-1E**), suggesting that **3e** either selectively binds to *apo* SLC1A1g or displaces bound Na^+.

To confirm the direct binding of **3e** to SLC1A1, we performed thermal shift binding assays using detergent-solubilized SLC1A1g. The protein was subjected to increasing temperature, and its unfolding was monitored using nano-differential scanning fluorimetry (nanoDSF). In a buffer containing 200 mM Na^+, SLC1A1g unfolded at ~69.1 ± 0.2°C. The

addition of 100 µM **3e** produced a modest increase in the melting temperature of ~0.4 ± 0.3°C (**Figures 1F and S2B**). In contrast, in Na^+-free, *apo* conditions, **3e** showed a more pronounced stabilization, with thermal shifts of ~1.8 ± 0.2°C (**Figure 1F and S2C**), suggesting binding. These findings are consistent with our earlier cellular thermal shift assays (CETSA), in which we detected direct **3e** binding using membrane-rich extracts from human RCC cells expressing high SLC1A1 levels.[3] A tighter binding in Na^+-free conditions is consistent with the structural data, suggesting that **3e** competes with Na^+ for binding.

Closer inspection of the transport domain structure reveals that in both structural classes, A and B, **3e** binds within a pocket formed between transmembrane (TM) helix 3 (TM3) and the N-terminal helix of the helical hairpin 2 (HP2) (**Figure 2A**). HP2 acts as a gate for substrate and ions accessing their binding sites.[39-43] HP2 closes upon binding of the substrate, three co-transported Na^+ (Na1-3) ions and a proton, or counter-transported K^+ ions (**Figure 1A**), facilitating the elevator-like movement of the transport domain. In the Na^+-bound and L-Glu-bound states, HP2 shifts closer to TM3, obstructing the **3e** binding pocket (**Figures 2B and 2C**). Notably, the drug-binding pocket remains accessible in the K^+-bound state (**Figure 2D**). TM3 harbors the conserved T101 and T102 residues, which, together with N366 and D368 in TM7, coordinate bound Na^+ in the Na3 site (**Figure 2E**). When bound, **3e** forms a water-mediated hydrogen bond between its aniline NH and the hydroxyl group of SLC1A1's T102 (**Figures 2F** and **2G**). Thus, **3e** and Na^+ in the Na3 site compete for the same T102 residue and favor different conformational states of the

transporter. These findings strongly suggest that **3e** prevents Na^+ – and, consequently, substrate – from binding the carrier.

Compound 3e and cholesterol bridge transport and scaffold domains.

In structural class A, we observed a well-resolved cholesterol molecule on the lipid-facing side of compound **3e** (**Figure 3A**). Its headgroup is adjacent to the TM2-TM3 loop that links the scaffold and transport domains on the cytoplasmic side, while the hydrophobic sterol moiety is nestled between the drug and the scaffold domain. In the dominant class B, this site is occupied by glyco-diosgenin (GDN) – a detergent used during protein purification (**Figure 3B**). Due to its larger size, GDN wedges more deeply into the crevice between the scaffold and transport domains, with its polar headgroup protruding beneath the TM2-TM3 loop. As a result, the transport domain swings slightly outward. In both structures, the hydrocarbon tails and parts of the sterol rings of cholesterol and GDN form intimate van der Waals contacts with **3e** on one side and the scaffold domain on the other. By contrast, no well-ordered lipid-like densities were observed at this site in the Na^+-bound IF SLC1A1g structure. These findings suggest that **3e**, together with the associated sterols, may bridge the two domains, impeding elevator-like domain movements and arresting the transporter in the IF state. A similar mechanism was proposed for UCPH-101, an allosteric, non-competitive SLC1A3/EAAT1-selective inhibitor,[44,45] which binds between the scaffold and transport domains in the OF state of SLC1A3 to prevent inward translocation of the transport domain[26] (**Figure 3C**).

Structural basis of 3e's SLC1A1 selectivity.

Most residues forming the **3e**-binding pocket are conserved across SLC1 paralogs, except for F99, which is unique to SLC1A1, and which interacts with ortho-methylaniline of **3e** (**Figure 3D**). To probe the role of the F99 residue, we mutated it to leucine or methionine – residues found at the equivalent position in other SLC1 paralogs (**Figure 3E**) – or to alanine as a control. Additionally, we mutated the conserved T402 residue, which forms a hydrogen bond with the core imidazopyridine ring of **3e**, to isoleucine or leucine. We evaluated these mutants using cell survival assays to assess **3e**-mediated inhibition of SLC1A1 and nanoDSF to assess direct binding to the transporter.

We first tested the functionality of the SLC1A1 mutants in a rescue assay. CRISPR/Cas9-mediated knockout of SLC1A1 (1A1sg5) causes antiproliferative effects in human kidney cancer cells, such as A498, but viability can be restored by introducing a sgRNA-resistant version of functional SLC1A1. Except for the F99A mutant, all F99 and T402 variants retained functionality and restored cell viability to levels comparable to wild-type (WT) SLC1A1 (**Figure 3F**). We then used these isogenic A498 cells expressing either WT or mutant SLC1A1, or GFP as a non-specific control, in the presence of endogenous SLC1A1 and cultured them with various doses of **3e**. All functional **3e**-binding site mutants resisted the cytotoxic effects of **3e**, whereas cells expressing WT SLC1A1, the non-functional F99A mutant, or GFP remained sensitive (**Figure 3G**). Notably, the latter two cell lines depend on endogenously expressed SLC1A1, which is inhibited by **3e**.

We also introduced the F99L and F99M mutations into SLC1A1g. Both purified mutant proteins remained monodisperse in size exclusion chromatography (**Figure S2D**) and exhibited thermal stability similar to WT in the nanoDSF assays, with *Ti* values of ~67.3 ± 0.5°C (F99M) and ~65.6 ± 1.8°C (F99L) (**Figures S2E and S2F**). However, **3e** failed to stabilize these mutant proteins (**Figure 3H**), consistent with substitutions at F99 disrupting **3e** binding. These results validate our cryo-EM structure and identify F99 as a key determinant of **3e**'s selectivity towards SLC1A1. Furthermore, these drug-resistant mutants confirm that **3e**'s cytotoxicity in kidney cancer cells is mediated through on-target inhibition of SLC1A1.

Structure-activity relationship (SAR) studies to identify new SLC1A1 blockers

Compound **3e** binds within a lipid-embedded hydrophobic pocket and, unsurprisingly, is itself highly hydrophobic with a cLogP of 5.4. The ortho-methylaniline moiety orients toward the selectivity-defining residue F99, while the 2-furanyl ring is positioned beneath the adjacent cholesterol molecule, engaging in an arene-H interaction with the sidechain of M367 and packing against I406 (**Figures 3A** and **3D**). This binding pose explains **3e**'s previously reported empirical SAR.[35] Decreasing **3e**'s overall lipophilicity by the addition of polar groups reduced its potency, likely due to compromised membrane penetration and inability to access the binding site. **3e** forms two hydrogen bonds with SLC1A1: one between the core N1 and the hydroxyl group of T402; and another – mediated by a well-resolved structural water – between the aniline NH and the hydroxyl of T102 (**Figures 2F** and **3D**). Consistent with this, removal of the N1 hydrogen bond acceptor substantially reduced **3e**'s inhibitory potency in the previous SAR.[35] The 8-bromo group of **3e** projects

into a narrow hydrophobic shelf formed by I399 and A371 in HP2, and V106 in TM3. These key interactions explain why the removal of C8-substituents disrupted binding. Finally, only the C7-position of the imidazopyridine core is partially exposed to solvent, which likely explains why bulky substitutions at other positions, particularly at C5 and C6, result in reduced activity due to steric clashes with the protein wall.

Guided by these structural insights, we identified four key groups, R_1-R_4, in **3e** that were amenable to modifications (**Figure S3A**) and designed a series of new BIA analogs. First, given potential concerns over the oxidative metabolism of the 2-furanyl group, we designed modifications that replaced this moiety (R_1). Second, we tested the possibility of replacing the aniline and phenyl substitutions at C3 (R_2). We maintained a hydrophobic moiety at the C8-position (R_3), preserving high cLogP, and retained the hydrogen bond with T402. We tested the possibility of introducing additional hydrophobic groups into the C7-position (R_4). Importantly, the buried C5- and C6-positions were left unsubstituted to avoid steric clashes. We computationally docked a virtual library of **3e** analog molecules into our cryo-EM structure and prioritized candidates with favorable poses and predicted free energies of binding lower than that of **3e**. Ultimately, we synthesized and evaluated ~40 BIA analogs (**Supplementary Tables 2** and **3**).

We screened the BIA compounds using two orthogonal approaches. First, we employed the nanoDSF assay to measure the ligand-induced thermal stabilization of SLC1A1g under Na^+-free conditions. As expected, **3e** stabilized the carrier by ~3.5ºC; however, vehicle control (DMSO), buffer control (N-methyl-D-glucamine, NMDG), and TFB-TBOA,

whose binding depends on Na^+, had no measurable effect (**Figure 4A**). The **3e** analogs exhibited a range of stabilizing effects, with 21 candidates increasing the melting temperature by at least 1°C (**Figures 4A** and **S3B**). Second, we assessed the cytotoxicity of the compounds in the SLC1A1-dependent A498 cells using a high-throughput 384-well format assay over 7 days. Compared to the earlier 12-well, 14–20-day assay (**Figure 3G**), the GI_{50} values were generally higher in the 384-well format, likely reflecting differences in assay duration and the metabolic state of the cells. Using **3e** as a reference, we identified ~20 analogs with greater potency (**Figure 4B**). From these, we selected the most potent compounds (**12**, **10**, **30**, **38**, and **04**; **Figures 4C** and **4D**) that also stabilized SLC1A1g by more than 1°C in the nanoDSF assays for further validation. As a negative control, we also included the highly cytotoxic compound **14**, which did not bind to SLC1A1g in the thermal shift assays (**Figure 4A**), suggesting it would display off-target (i.e., non-SLC1A1-mediated) cytotoxicity.

Identifying improved SLC1A1-selective BIA analogs

We first tested the selected analogs in two additional human RCC lines, UMRC-2 and 786O, which are less sensitive to SLC1A1 inhibition than A498 cells. Two compounds – **30** (featuring the C2-azetidine and C7-fluoro substitutions, hereafter referred to as PBJ1) and **38** (containing a C8-difluoromethyl substitution, hereafter referred to as PBJ2) – demonstrated increased cytotoxicity in these cells compared to **3e** (**Figures 5A - 5C**). When docked into the cryo-EM structure, both PBJ1 and PBJ2 occupied the **3e** binding pocket in poses virtually identical to **3e**, while extending into adjacent available cavities (**Figure 5D**). Expressing drug-resistant SLC1A1 F99M and T402I mutants in A498 cells

conferred resistance to PBJ1 and PBJ2 (**Figure 5E**), mirroring their resistance to **3e** (**Figure 3G**). In contrast, other tested analogs showed no improvements in potency in UMRC2 and 786O cells (**Figures S4A** and **S4B**) and were cytotoxic for A498 cells expressing the drug-resistant mutants (**Figures S4C**-**S4H**), suggesting that they might have off-target effects. Altogether, we discovered two new analogs – PBJ1 and PBJ2 – that are more potent on-target derivatives of **3e**.

To directly assess inhibition of SLC1A1's transporter activity, we measured cellular impedance. L-Asp and L-Glu uptake causes cellular swelling and increased impedance (**Figure 6A**).[46] We generated monoclonal HEK293 cells with doxycycline (Dox)- inducible expression of SLC1A1, SLC1A2, or SLC1A3 (**Figure 6B**). HEK293-SLC1A1 cells demonstrated a time-dependent increase in impedance in the presence of L-Glu, reaching equilibrium at ~1 hour after substrate addition (**Figures 6C and S5A**-**S5B**). Notably, these changes occurred only in the presence of Dox, which aligns with previous reports of low endogenous expression of SLC1 transporters in the HEK293 cells,[46] demonstrating their suitability for these impedance-based uptake assays. Compound **3e** inhibited the uptake of 1 mM L-Glu (**Figures 6C and S5B**), 2 mM L-Glu (**Figure S5C**), and 2 mM L-Asp (**Figure S5D**), in a dose-dependent manner. In these assays, PBJ1 and PBJ2 showed IC_{50} values of ~10 μM, comparable to **3e**, while retaining >100-fold selectivity against SLC1A2 and SLC1A3 (**Figure 6D)**. By contrast, TFB-TBOA, a competitive pan-SLC1 inhibitor,[34] blocked uptake by all subtypes (**Figure 6D**). Thus, PBJ1 and PBJ2 retain the SLC1A1 selectivity of the parent **3e** compound.

Metabolic contribution of the SLC1A1 inhibitors in kidney cancer cells

The three amino acids imported by SLC1A1 – L-Asp, L-Glu, and L-Cys – are precursors for critical metabolites in cancer cells. L-Asp provides the carbon skeleton for nucleotide biosynthesis; both L-Asp and L-Glu contribute towards the tricarboxylic acid (TCA) cycle; and L-Glu and L-Cys are precursors for glutathione (reduced: GSH; oxidized: GSSG) biosynthesis (**Figure 7A**). Consistently, treating A498 cells with **3e**, PBJ1, and PBJ2 reduced intracellular pools of GSH and GSSG (**Figures 7B and 7C**), in line with our previous metabolomics data showing a prominent reduction in TCA cycle metabolites and GSH/GSSG following **3e** treatment in kidney cancer cells.[3] Moreover, the reduction in GSH/GSSG levels correlated with the antiproliferative effects of these compounds (**Figures 7B** - **7D**). Finally, supplementation with cell-permeable methyl ester derivatives of L-Asp (meAsp), L-Glu (meGlu), or GSH rescued the fitness defects caused by PBJ1 and PBJ2 (**Figures 7E** - **7G**). These findings support the conclusion that the antiproliferative activity of BIAs arises from metabolic perturbations directly linked to the inhibition of SLC1A1.

Discussion

The SLC1 family includes five dicarboxylic acid transporters, EAATs, which differ in tissue distribution and physiological roles.[47-50] All are expressed in the CNS, where SLC1A2/EAAT2 and SLC1A3/EAAT1 are primarily responsible for clearing synaptic L-Glu; their diminished activity leads to devastating neurological pathologies. SLC1A1/EAAT3's broader expression in peripheral tissues distinguishes it among EAATs. In the kidney, it mediates the reabsorption of L-Glu and L-Asp, becoming critical for

sustaining the metabolic demands of kidney cancer cells. This metabolic reliance on SLC1A1 credentials this transporter as a promising therapeutic target, underscoring the need for SLC1A1-selective inhibitors.

Developing subtype-selective drugs for EAATs has been challenging because of the high conservation of their substrate-binding sites. Recent cryo-EM structures of SLC1A1-3 confirmed that these sites are nearly identical across paralogs, limiting the selectivity of orthosteric competitive inhibitors.[26-31,51] Moreover, such compounds are often ineffective under physiological conditions where substrate concentrations are high. In contrast, allosteric SLC1 inhibitors, such as the SLC1A3/EAAT1-selective UCPH-101,[44,45] hold greater therapeutic promise because they target less conserved sites and often act via non-competitive mechanisms, enabling subtype selectivity and sustained efficacy.

Growing recognition of SLC1A1's role in human disease has spurred efforts to develop selective inhibitors, leading to the discovery of the BIA series, including compound **3e**.[35] However, the structural basis for **3e**'s SLC1A1-selective inhibition remained unresolved. Our high-resolution cryo-EM structure revealed that **3e** binds to SLC1A1 in its IF *apo* state, outside of the substrate-binding site. It engages a membrane-embedded allosteric pocket and, together with a cholesterol molecule, wedges between the transport and scaffold domains. This binding mode resembles that of UCPH-101, which binds to the SLC1A3 transporter in its OF conformation at the domain interface and is thought to inhibit transport by blocking the elevator movements of the transport domain. By analogy, **3e** may similarly block elevator movements, arresting the transporter in the IF state.

However, unlike UCPH-101, **3e** also interferes with ion and substrate binding by engaging a residue involved in Na^+ coordination. Prior structural studies have shown that SLC1A1 functions as a highly dynamic molecular machine, undergoing complex structural changes during its transport cycle (**Figure 1A**).[29-31] **3e** selectively targets just one of these states, underscoring the importance of considering the full conformational landscape of SLC1 and other dynamic membrane transporters in the development of next-generation inhibitors.

Our structures further revealed that the F99 residue, which is not conserved in other SLC1 transporters, is the determinant of subtype selectivity. Mutating F99 produced functional transporters that could not bind **3e**. These mutants, as well as mutants of T402, which is intimately involved in drug coordination, confer resistance to compound-induced cell death in RCC cell lines. These drug-resistant mutants are a gold-standard tool to demonstrate that **3e,** and newly identified PBJ1 and PBJ2 analogs, act on-target in cellular assays. Consistently, metabolic rescue experiments revealed that PBJ1 and PBJ2 prevent cancer cell growth by directly blocking SLC1A1-mediated amino acid uptake.

PBJ1 and PBJ2 compounds emerged from our structure-guided SAR campaign. Interestingly, while they showed improved on-target cytotoxicity compared to **3e** in cell assays, they did not exhibit increased affinity for SLC1A1 in nanoDSF or higher inhibitory potency in the impedance-based transport assays. This might be because the antiproliferative assays measure the impact of sustained SLC1A1 blockade over a period of 2-3 weeks. In contrast, the other assays measure more acute effects occurring on time

scales of minutes to hours. Moreover, unlike other approaches, antiproliferative assays measure the cumulative impact of blocking the uptake of all SLC1A1 substrates. Altogether, binding and inhibition assays can identify *bona fide* SLC1A1 inhibitors but might not perfectly capture the analog's cellular potency.

PBJ1 and PBJ2 have improved certain pharmacological features over the parental **3e** molecule. For instance, PBJ1 lacks the labile furan ring, whereas PBJ2 has the methyl-difluoro replacement for bromine, which improves its 'drug-like' features. Given the membrane-embedded nature of the binding pocket, further optimization of these BIA inhibitors might prove challenging. Nevertheless, our findings provide the structural basis and the rigorous validation pipeline necessary for a more comprehensive search for future discovery of new chemical scaffolds that target SLC1A1.

Data Availability

All the data necessary to evaluate the conclusions of the manuscript are provided in the paper and/or the Supplementary Materials. The Cryo-EM maps and atomic coordinates have been deposited in the Electron Microscopy Data Bank (EMDB) and Protein Data Bank (PDB) under accession codes: EMD-71288, PDB-9P4X (SLC1A1g protomer with **3e** and cholesterol, class A); EMD-71289, PDB-9P4Y (SLC1A1g protomer with **3e** and GDN, class B); EMD-71290, PDB-9P4Z (Na^+-bound SLC1A1g protomer).

Acknowledgments

We thank Carl Fluck at the Weill Cornell Medicine Electron Microscopy facility for the initial grid screening and preliminary data collection, and Robert Grassucci, Zhening Zhang, and Yen-hong Kao at Columbia University Cryo-Electron Microscopy Center for high-resolution data collection. This work was supported by the following grants to A.A.C.: seed money from the Cleveland Clinic Foundation, the DoD's KCRP-ECI award (W81XWH-20-1-0804), and the Velosano pilot award. PK was supported by a postdoctoral fellowship from Velosano. JAC, NSW, TR, CMG and SRS were supported by funds from Shared Laboratory Services at the Lerner Research Institute. OB was supported by HHMI and the National Institute of Neurological Disorders and Stroke (R37NS085318).

Author Contributions

Conceptualized, designed, and analyzed experiments: PK, BQ, JAC, AE, NSW, TR, CMG, SRS, OB, AAC; ***Performed experiments:*** PK, BQ, JAC, AE, NW, TR; ***Wrote the manuscript:*** PK, BQ, JAC, SRS, OB, AAC.

Declaration of Interests

The authors declare no conflicts of interest with the work presented in this manuscript.

Methods

Protein expression and purification

The de-glycosylation (N178T, N195T) mutant of human SLC1A1/EAAT3 protein, termed SLC1A1g for short, was purified as previously described.[29-31] In brief, 1L suspension FreeStyle™ 293-F cells at a density of 2.5 million cells per mL were transiently transfected with 3 mg DNA and 9 mg PEI 25K (*Polysciences*). The cells were harvested after 48 hours post-transfection and resuspended in lysis buffer containing: 50 mM Tris-HCl (pH 8.0), 1 mM EDTA, 1 mM L-Asp, 1 mM tris (2-carboxyethyl) phosphine (TCEP), 1 mM phenylmethylsulfonyl fluoride (PMSF), and 1:200 dilution of protease inhibitor cocktail (catalog no. P8340, *Sigma-Aldrich*). The cells were disrupted using an EmulsiFlex-C3 homogenizer (*Avestin*) and the cell debris was removed by centrifugation at 10,000g for 15 min at 4°C. The membrane pellets were collected by ultracentrifugation at 186,000g for 1 hour at 4°C and solubilized in lysis buffer supplemented with 200 mM NaCl, 10% glycerol, 1% dodecyl-β-D-maltopyranoside (DDM, *Anatrace*), and 0.2% cholesteryl hemisuccinate (CHS; *Sigma-Aldrich*) overnight at 4°C. The insoluble material was removed by centrifugation at 10,000g for 30 minutes at 4°C; the supernatant was then incubated with Strep-Tactin Sepharose resin (*GE Healthcare*) for 1 hour at 4 °C. The resin was washed with 8 column volumes of buffer containing 50 mM Tris-HCl (pH 8.0), 200 mM NaCl, 1 mM L-Asp, 1 mM TCEP, 5% glycerol, and 0.06% glyco-diosgenin (GDN, *Anatrace*), and the protein was eluted with 4 column volumes of the same buffer supplemented with 2.5 mM D-desthiobiotin (*Sigma-Aldrich*). The N-terminal Strep II and GFP tags were cleaved by incubating the protein with Prescission protease overnight at 4°C at a 40:1 w:w ratio. The protein was further purified in "*apo*" condition by size-

exclusion chromatography (SEC) in a buffer containing: 20 mM HEPES-Tris (pH 7.4), 100 mM N-methyl-D-glucamine (NMDG) chloride, 1 mM TCEP, and 0.01% GDN.

Thermostability assays

Purified Apo SLC1A1g was concentrated to ~100 µM and then diluted 20-fold in a buffer containing 50 mM Hepes-Tris pH 7.4, 100 mM NMDG-Cl, and 0.01% GDN, without or with supplementation with 100 µM **3e** or other drugs dissolved in DMSO. During the screening of **3e** analogs, the final mixtures contained 10% DMSO, whereas in the initial **3e** binding experiments, the DMSO concentration was 1%. NMDG-Cl was 200 mM in these experiments. The thermostability assay was performed using Tycho NT.6 (*NanoTemper Technologies*). In brief, protein samples were heated from 35°C to 95°C at a rate of 30°C per minute, and the intrinsic fluorescence of the protein was recorded at 330 nm and 350 nm. The amplitude ratio of A350/A330, its first derivative, and the inflection temperature (*Ti*) were calculated by the Tycho NT.6 software. All measurements were repeated at least three times.

Cryo-EM sample preparation and data acquisition

Purified *apo* SLC1A1g was supplemented with 200 mM NaCl and 100 µM compound **3e** and concentrated to about 4 mg/ml at room temperature. 3.5 µl sample was applied to glow-discharged QUANTIFOIL R1.2/1.3 holey carbon-coated 300 mesh gold grids (*Quantifoil*, *Großlöbichau*). The grids were blotted for 3 seconds at room temperature and 100% humidity and plunge-frozen into liquid ethane using a Mark IV Vitrobot (*FEI*). The cryo-EM dataset was auto-collected using Leginon[52] on Titan Krios equipped with a 20

ev energy filter and Gatan K3 camera at the Columbia University Cryo-Electron Microscopy Center. A total of 9,970 movies were collected at a nominal magnification of 100,500-fold with a calibrated pixel size of 0.83 Å in counting mode. A nominal defocus value of -1.0 – -2.0 µm and a total dose of 58 $e^-/Å^2$ over 50 frames were applied to the data collection.

Cryo-EM image processing

The cryo-EM dataset was processed using a combination of Relion 3.1.0[53] and CryoSPARC v4.2.1[54] software packages. The movies were aligned using Motioncor2 in Relion, and the micrographs were imported into CryoSparc. The CTF parameters of the micrographs were estimated using Path CTF, and micrographs with the CTF fit resolution worse than 6 Å were removed from the dataset. About 6.7 million particles were picked from 9,594 images, and ~2.7 million particles were extracted using a box size of 160 pixels with 2x binning after particle inspection. The particles were subjected to 2D classification, and 945 K particles exhibiting secondary structure features were selected and subjected to two rounds of *ab initio* reconstructions. 303 K particles producing a volume with the most features were further refined to 3.4 Å by nonuniform refinement (hereafter, NUR) with C1 symmetry. Separately, 162 K particles extracted from 500 micrographs were subjected to 1–10 iterations of *ab initio* reconstructions to generate 5 decoy volumes. After removing obvious nonprotein junk particles in the 2D selection step, about 2.5 million particles were subjected to heterogeneous refinement using one good volume (3.4 Å from the last step NUR) and 5 decoy volumes for cleaning (heterogeneous refinement cleaning, HRC). After that, 589 K selected particles were re-extracted with a

box size of 320 pixels without binning and subjected to HRC with C1 and NUR with C3 symmetry. Then, the particles were imported into Relion using PyEM (doi.org/10.5281/zenodo.3576630) for polishing. The polished particles were reimported into CryoSparc and subjected to HRC and NUR. After 2 rounds of polishing, HRC, and NUR steps, 556 K particles were refined to 2.46 Å using C3 symmetry. Symmetry expansion and local classification were performed in CryoSPARC, with a mask applied over the protomer to resolve conformational heterogeneity. Three protomer conformations were further locally refined to 2.56 Å (IF apo with **3e** and GDN-bound conformation), 2.76 Å (IF apo with **3e** and cholesterol-bound conformation), and 2.83 Å (IF Na^+-bound conformation) in CryoSPARC.

Model building and refinement

The IF *apo* and Na^+ ion bound SLC1A1g structures (PDB codes: 6X3F, and 6X2L, respectively) were fitted into EM density maps using ChimeraX.[55] The models were manually adjusted in COOT[56] and subjected to real-space refinement in Phenix.[57] Structural model validation was performed in Phenix, and structural figures were prepared using ChimeraX. The Cryo-EM maps and atomic coordinates have been deposited in the Electron Microscopy Data Bank (EMDB) and Protein Data Bank (PDB) under accession codes: Class A, (IF *apo* with compound **3e** and cholesterol bound, EMD-71288, PDB-9P4X); Class B, (IF *apo* with compound **3e** and GDN bound, EMD-71289, PDB-9P4Y); and Class C, (IF Na^+ bound, EMD-71290, PDB-9P4Z).

Cell lines

A-498 (RRID: CVCL_1056), HEK293T (RRID: CVCL_0063), and 786-O (RRID: CVCL_1051) cells were obtained from the American Type Culture Collection. UMRC-2 (RRID: CVCL_2739) cells were obtained from Dr. Bert Zbar and Dr. Marston Linehan (National Cancer Institute). All cells were maintained in Dulbecco's Modified Eagle's Medium (DMEM) (Life Technologies 11995073) supplemented with 10% Fetal Bovine Serum (FBS) (Life Technologies 10437-028), and 1X Penicillin-Streptomycin (Life Technologies 15140163). Cells stably expressing cDNAs or sgRNA were generated by lentiviral infection followed by selection with Puromycin (2 µg/mL) or Blasticidin (10 µg/mL), as appropriate. HEK293$^{SLC1A1/SLC1A2/SLC1A3}$ cell lines were cultured in high-glucose Dulbecco's Modified Eagle Medium (DMEM, CCF Media Core) supplemented with 10% heat-inactivated Fetal Bovine Serum (FBS) (Gibco A5256801), 5 U/mL Penicillin/Streptomycin (Sigma P3032 & Gibco 11860), 2 mM L-glutamine (CCF Media Core), and 0.8 mg/mL puromycin (Phytopure^{TM}, MP Biomedicals 0219453925). All cells were grown at 37°C in 5% CO_2.

Lentiviral Infections

Lentiviral particles to introduce cDNAs or sgRNAs into cells were produced from HEK293T packaging cells. In a standard experiment, we seeded ~1.6E06 - 2.0E06 HEK293 cells into a 6 cm dish and transfected these cells with a transfection mix that contained 3 µg total DNA [1.5 µg lentiviral plasmid + 1.5 µg helper plasmids - psPAX2 (RRID: Addgene_12260) and pMD2.G (RRID: Addgene_12259) mixed in a 3:1 ratio] and 9 µl lipofectamine 2000 (Invitrogen 11668019). The transfection mixtures were prepared

and incubated at RT for 20 minutes and then added dropwise onto cells. Cells were incubated for sixteen hours, following which the media was changed. Viral supernatant was collected at 48- and 72-hours post-transfection, combined, and filtered (0.45 µm). Aliquots were stored frozen at -80°C. To transduce recipient cells, we seeded 6-well plates with 1.5E05 - 2.0E05 cells and transduced them with 0.5 mL of the lentiviral supernatant in the presence of 8 µg/mL polybrene. The plates were returned to the incubator for 16 hours, after which the media was replaced, and cells were grown for an additional 24 hours prior to selection with the appropriate antibiotic.

Generation of SLC1A1 Mutant Constructs

Entry vectors and pLX304 constructs encoding sg5-resistant versions of SLC1A1 were previously described.[3] Mutations encoding F99A, F99M, F99L, T402I, and T402L were generated in the sg5-resistant backbone either using overlap-extension PCR or by site-directed mutagenesis (Quickchange II XL; Agilent 200521) using the oligos described in the primer list. All mutant clones were verified by Sanger sequencing. Engineered clones were lentivirally transduced into recipient cells using the procedures described above. For the genetic rescue experiments to assay SLC1A1 functionality, cells were first engineered to express the sgRNA-resistant versions of either WT or mutant SLC1A1 (or GFP, as a control) in the pLX304 backbone (RRID: Addgene_25890). Following selection with blasticidin (10 µg/mL, 7-10 days), cells were lentivirally transduced with CRISPR/Cas9 constructs targeting SLC1A1 (1A1sg5) or a non-targeting control and selected with puromycin (2 µg/mL, 3 days). The sgRNA sequences are provided in the primer list. Following the second selection, equal number of viable cells were seeded at low density

(typically, 100-200 cells/well of a 12-well plate) and cultured for 1-2 weeks post selection before staining the wells with crystal violet (0.25% in 20% methanol, stained overnight at 4˚C).

Primer List

Mutagenesis Primers

Name	Mutation	Sequence
1A1F99Atop	F99A	GCTGTCGTGTATTATGCCTGTACCACTCTCATT
1A1F99Abtm	F99A	AATGAGAGTGGTACAGGCATAATACACGACAGC
1A1F99Mtop	F99M	GCTGTCGTGTATTATATGTGTACCACTCTCATT
1A1F99Mbtm	F99M	AATGAGAGTGGTACACATATAATACACGACAGC
1A1F99Ltop	F99L	GCTGTCGTGTATTATTTATGTACCACTCTCATT
1A1F99Lbtm	F99L	AATGAGAGTGGTACATAAATAATACACGACAGC
1A1T402Itop	T402I	ATCAGTATCACGGCCATATCTGCCAGCATCGGA
1A1T402Ibtm	T402I	TCCGATGCTGGCAGATATGGCCGTGATACTGAT
1A1T402Ltop	T402L	ATCAGTATCACGGCCTTATCTGCCAGCATCGGA
1A1T402Lbtm	T402L	TCCGATGCTGGCAGATAAGGCCGTGATACTGAT

sgRNA sequences

Name	Target Gene	Sequence
CT110 (sgCon)	Non-Targeting	GGAGGCTAAGCGTCGCAA
1A1sg5	*SLC1A1*	TCACCTGATGAGATCTAACA

High Throughput Screening Assay for Compound 3e and Its Analogs

A two-fold serial dilution of each test compound was prepared in 100 % DMSO starting at 25 mM. White tissue culture 384-well plates were first pre-filled with 30 µL of complete DMEM with 1 mM L-Glu. Next, 100 nL of each compound dilution was acoustically dispensed into the plates in triplicate with a Labcyte Echo 550; vehicle (0.2 % DMSO final) and compound **3e** served as negative and positive controls, respectively. Finally, A 498 were seeded by adding 20 µL of a 2.5×10^4 cells /mL suspension (≈ 500 cells per well) using an E1 ClipTip electronic multichannel pipette, bringing the total well volume to 50 µL while maintaining 0.2 % DMSO. Plates were incubated for seven days at 37°C, 5 % CO2. Cell viability was measured by adding 25 µL CellTiter Glo® 2.0 reagent (Promega G7571) to each well, shaking for five minutes at 600 rpm, incubating ten minutes at room temperature, and recording luminescence on a Revvity EnVision multimode plate reader. Luminescence in the vehicle-treated wells was normalized to 100% and used to perform regression analysis and establish each inhibitor's GI50, using the built-in algorithms in Graphpad prism (e.g., log-inhibitor versus response – variable slope).

Cytotoxicity assays using SLC1A1 Inhibitors

Cytotoxicity assays were used to evaluate the potency and on-target effects of the new SLC1A1 inhibitors (Cmpd **3e** analogs). To compare potency in human clear cell Renal Cell Carcinoma (ccRCC) cell lines, such as A 498, UMRC2, and 786 O, cells were seeded into 96 well plates (200 cells/well in 100 µL DMEM) and allowed to attach overnight. Serial two-fold dilutions of each test inhibitor were prepared in 100 % DMSO and diluted into complete medium to yield final inhibitor concentrations between 0.8 to 50 µM, each in

0.1 % (v/v) DMSO. Overnight culture media was aspirated and 200 µL of the appropriate drug containing media was gently added to each well.

To test on-target effects of each inhibitor, A-498 cells expressing either wild-type, F99M, or T402I SLC1A1 mutants (or GFP expressing controls) were seeded (100 cells/well in 1 mL volume) in a 12 well tissue culture plate. After 16 h to allow attachment, cells were exposed either to test compounds (final concentrations as indicated) or to 0.1 % (v/v) DMSO vehicle (negative control). The medium—including fresh compound or DMSO—was replaced every three days to ensure continuous treatment. After 21 days, colonies were trypsinised and viable cell numbers were counted using a Vi-Cell to assess the effects of treatment. Three independent biological replicates were statistically compared.

For metabolic rescue experiments, 3.0E05 A-498 cells were cultured in the presence of esterified L-Asp (meAsp, 100 µM), esterified L-Glu (meGlu, 100 µM), reduced Glutathione (GSH, 1 mM), or untreated (controls) for 3 days. The cells were then trypsinized, counted, and reseeded (1000 cells /well in a 12 well plate). The cells were cultured in the presence of the indicated supplements (or untreated controls) and PBJ1 or PBJ2 (0, 1.5, 3.0, or 6.0 µM for 2-3 weeks with media changes every 3-4 days. Fresh inhibitor and metabolite supplements were added at each media change. Cell counts were measured using the Vi-Cell counter and three independent biological replicates were statistically compared to evaluate differences.

Generation of HEK293$^{SLC1A1/SLC1A2/SLC1A3}$ Monoclonal Cell Lines

Full-length, human, mammalian codon-optimized SLC1A1 (#161044), SLC1A2 (#161067), and SLC1A3 (#161055) entry clones were obtained from AddGene. The SLC1Ax coding sequences were PCR amplified with compatible overhangs and cloned by a HiFi assembly (NEB) into a custom pPB-TetOn-Puro-SLC1Ax/3xGS/3xFLAG_SLC1Ax/P2A/EGFP (Vector Builder). This construct allows stable integration, via the PiggyBac® system, of a Dox-inducible SLC1Ax-3xFLAG cassette alongside a post-translationally released (P2A) EGFP. All three constructs were confirmed by whole-plasmid sequencing (Plasmidsaurus).

Parental HEK293T cells were co-transfected with pPB-TetOn-Puro-SLC1Ax/3xGS/3xFLAG_SLC1Ax/P2A/EGFP plasmids and SPB-DNA (Hera Biolabs) at a 3:1 ratio with Fugene HD (Promega) per manufacturer's instructions. After 24 hours, the transfection media was replaced with full cell culture media supplemented with 0.8 mg/mL puromycin, and stably transfected pools were established after 5 days of selection.

For the establishment of monoclonal lines, each SLC1Ax selected pool was first enriched for high doxycycline-induced GFP expression by flow sorting using a ThermoFisher Bigfoot Spectral Cell Sorter. Each pool was seeded in full cell culture media in 2 T-175 flasks. At 80% confluence, cells were treated with 0.15 mg/mL doxycycline or vehicle for 24 hours. $3x10^7$ cells were harvested from each flask and resuspended to $1x10^7$ cells/mL in cell sorting buffer: 1X Phosphate buffered saline (Ca^{2+}/Mg^{2+} free), 1 mM EDTA, 25 mM HEPES pH 7.0, 1% FBS. A separate T-75 flask of parental HEK293T cells was also

harvested and resuspended in cell sorting buffer to facilitate the definition of the (+) GFP gate. The top 4-6% GFP-expressing cells within the (+) GFP gate were sorted and plated at 1 cell/well in full cell culture media supplemented with 0.8 mg/mL puromycin in 96-well plates. 10-15 clones each for SLC1A1, SLC1A2, and SLC1A3 were expanded to T-75 flasks and tested for responsiveness in cell impedance measurements upon addition of 1 mM L-glutamate. SLC1A1 Monoclonal #6, SLC1A2 Monoclonal #5, and SLC1A3 Monoclonal #1 were used in reported impedance assays.

Impedance Assay

The impedance assay was conducted as previously described.[46] Briefly, HEK293^{SLC1A1}, HEK293^{SLC1A2}, and HEK293^{SLC1A3} monoclonal lines were passaged in complete DMEM media (2 mM L-glutamine). On Day 1 of the assay, a modified assay media containing DMEM with only 1 mM (0.5X) L-glutamine was prepared, and 50 µL was added to each well of an E-Plate 96 PET plate (Agilent, 300600910) and allowed to incubate at room temperature for at least 30 minutes. HEK293^{SLC1Ax} cells were split as standard into assay media and further diluted to a final concentration of 1.2 x 10^6 cells/mL. Once the cells were prepared, the E-Plate containing only media was placed in an xCELLigence RTCA (Agilent), and a background reading was taken. The plate was removed from the block, and 50 µL of cell suspension was added to each well, at a final concentration of 60,000 cells/well in 100 µL of assay media. Cells were incubated at room temperature for 30 minutes and then placed back onto the xCELLigence overnight. Readings were taken every 5 minutes until the completion of the assay.

On the morning of Day 2, a 450 ng/mL solution of doxycycline was prepared by adding 0.675 µL of a 10 mg/mL DMSO stock of doxycycline to 15 mL of DMEM complete media containing 10% FBS, 50 I.U. pen/strep, but without L-glutamine. 50 µL of doxycycline was added to a final concentration of 150 ng/mL, and SLC1Ax induction was allowed to proceed for 6-8 hours. Compound serial dilutions (1:2 in 100% DMSO) were prepared at a 1,000X top dose. 0.8 µL of the serially diluted compounds were added to 200 µL of L-glutamine-free assay media and mixed well. 50 µL of the compounds diluted in media (now 4X) were then added to the plate in technical duplicates. To columns 1 and 12, media containing the equivalent amount of DMSO was added, and the plate was returned to the xCELLigence overnight.

After 16 to 20 hours (Day 3), 10 µL of a 21mM (21X) PBS stock of L-glutamate (Sigma Aldrich 49621) was prepared fresh and added to a final concentration of 1 mM to columns 2 through 12. 10 µL of PBS only was added to column 1 as a vehicle control. For the comparison of L-Glu vs. L-Asp, a 42 mM stock was prepared, and the final concentration of agonist was 2 mM. The E-Plate was returned to the xCELLigence, and readings were continued for three hours post-stimulation.

For data analysis, raw cell index (CI) values were normalized to time = 0 (the last reading before L-Glu addition) within each well, and then the background vehicle response in PBS-stimulated cells (column 1) was subtracted to generate nCI values. The AUC from the nCI time-course (over 3 hours) was extracted and plotted against log[compound] to

extract IC_{50} values by non-linear regression using GraphPad Prism (v10). The maximum response in L-Glu stimulated cells (column 12) was set as the top of the curve.

Glutathione Detection

Glutathione measurements were done as per the manufacturer's instructions (Thermo Fisher Glutathione Colorimetric Detection Kit, Cat. # EIAGSHC). Briefly, A-498 cells (1.5E05 in a 10 cm dish) were treated with either Cmpd **3e**, PBJ1, or PBJ2 [each at 5 μM in 0.1 % (v/v) DMSO (vehicle control)] for 5 days. Cells were washed once with 1X PBS, trypsinized, and then harvested (300g, 5 min, 4 °C). Equal number of viable cells (5.0E05 per condition) were transferred to pre chilled tubes, washed once in ice cold 1X PBS and immediately deproteinised in ice cold 5% sulfosalicylic acid (SSA). Cell lysates, generated by vortexing and sonication (3" pulse at 30% amplitude), were incubated on ice for 10 mins and then clarified (14,000xg, 10 min, 4°C). The supernatant was split into two pre-chilled tubes to measure total (GSH) and oxidized (GSSG) glutathione levels.

GSH samples were processed directly, whereas GSSG samples were treated with 2 vinylpyridine (2VP; 5 μL 2VP solution per 250 μL lysate) for 1 h at room temperature to derivatize free thiols and leave only oxidized glutathione. Both samples were first diluted 1:5 with Assay Buffer (final 1% SSA) and then another time at 1:4 with Sample Diluent buffer (final 1:20 dilution). 50 μL diluted samples were combined with 25 μL Colorimetric Detection Reagent and 25 μL Reaction Mixture (NADPH + glutathione reductase). Plates were mixed gently and incubated 20 min at room temperature, then read at 405 nm on a SpectraMax i3 microplate reader. In parallel, a standard curve was generated for GSH

(0–25 μM) and GSSG (0 - 12.5 μM) and used to calculate absolute concentrations of GSH and GSSG in the cell lysates.

Procedures for the Synthesis of Cmpd 3e and Analogs

General Scheme.

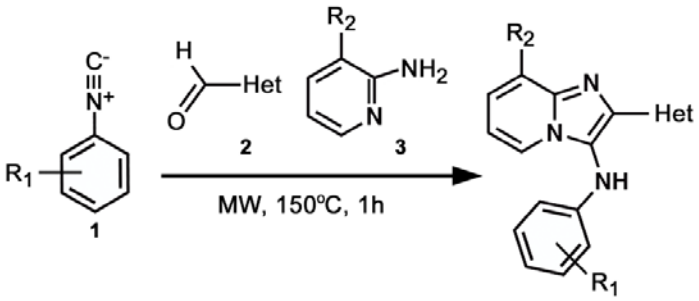

Synthesis of SLC1A1 (EAAT3) imidazopyridine cmpd **3e** and analogs reported herein were prepared according to the microwave irradiation protocol reported by Wu et al.[35] Procedures, characterization data, and purity are provided for compounds **4**, **10**, **12**, **14**, **30** (PBJ1), **38** (PBJ2). Additional analogs outside these compounds were prepared following a similar condensation microwave heating protocol, beginning with commercial or known isocyanides 1, aldehydes 2, and aminopyridines 3. The final imidazopyridines **1-38** had analytical purity >95% as judged by LC-MS and 1H NMR.

8-Bromo-2-(1H-pyrazol-3-yl)-N-(o-tolyl)imidazo[1,2-a]pyridin-3-amine (4).

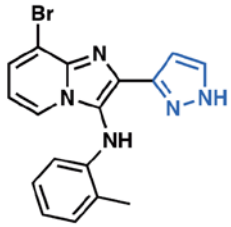

In a microwave reaction vial 1-isocyano-2-methylbenzene (102 mg, 0.87 mmol, 1.0 eq), 1*H*-pyrazole-3-carbaldehyde (84 mg, 0.87 mmol, 1.0 eq), and 3-bromopyridin-2-amine (150 mg, 0.87 mmol, 1.0 eq) were combined. The mixture was stirred neat at 160ºC for 1 h under microwave radiation. The crude product was purified by silica gel chromatography to give 8-bromo-2-(1H-pyrazol-3-yl)-*N*-(*o*-tolyl)imidazo[1,2-*a*]pyridin-3-amine (51.3 mg, 16%) as yellow solid: LCMS (ESI): m/z = 368.0, $[M+H]^+$, R_t = 1.495 min; >95% (210, 254 nm); ^{1}H NMR (400 MHz, DMSO) δ 12.5 (m, 1H), 8.19 (s, 1H), 7.72 (d, J = 6.8 Hz, 1H), 7.50 (s, 1H), 7.14 (d, J = 6.8 Hz, 1H), 6.87 (dt, J = 14.5, 7.0 Hz, 2H), 6.69 (t, J = 7.4 Hz, 1H), 5.90 (d, J = 8.0 Hz, 1H), 2.40 (s, 3H).

<u>8-Bromo-2-(furan-2-yl)-*N*-(*m*-tolyl)imidazo[1,2-*a*]pyridin-3-amine (10).</u>

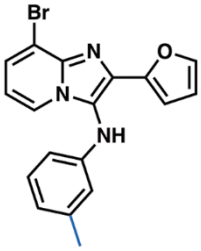

Step 1. Preparation of N-m-tolylformamide.

A mixture of 3-methoxyaniline (2 g, 18.7 mmol, 1 eq), formic acid (30 mL), and sodium formate (12.7 g, 186.6 mmol, 10 eq) in a 100 mL round-bottom flask was stirred with a magnetic stir bar at room temperature. The progress of the reaction was monitored by TLC. When the reaction reached completion, 30 mL of EtOAc was added into the system, and the organic solvent was then washed with H_2O (3 × 50 mL) and a saturated solution of $NaHCO_3$(50 mL). After drying with Na_2SO_4, the solvent was removed under reduced pressure. The resulting residue (890 mg, 35%) containing the *N*-*m*-tolylformamide was

taken on to the next step without additional purification: LCMS (ESI): m/z = 152.0, $[M+H]^+$, R_t = 0.635 min; >90% (210, 254 nm).

Step 2. Preparation of 1-isocyano-3-methylbenzene.

To a solution of *N*-*m*-tolylformamide (800 mg, 5.92 mmol, 1 eq) and Et_3N (1.98 g, 19.53 mmol, 3.3 eq) in anhydrous DCM (10 mL) was added dropwise $POCl_3$ (998.2 mg, 6.51 mmol, 1.1 eq) at 0 ^oC under a nitrogen atmosphere over 35 min. Then the reaction mixture was stirred at 0 ^oC for 1 h. After completion, the reaction mixture was poured into a saturated solution of $NaHCO_3$ at 0 ^oC. The mixture was extracted by DCM. The organic phase was dried over Na_2SO_4 and the solvent was removed under reduced pressure. The crude product was purified by silica gel column chromatography to give the title product as a yellow green liquid (600 mg g, 86%) which was used directly in step 3 without further purification.

Step 3. Procedure for preparation of 8-bromo-2-(furan-2-yl)-N-(m-tolyl)imidazo[1,2-a]pyridin-3-amine.

To 1-isocyano-3-methylbenzene (203.1 mg, 1.73 mmol, 1.0 eq) from step 2, furan-2-carbaldehyde (166.6 mg,1.73 mmol, 1.0 eq), and 3-bromopyridin-2-amine (300 mg, 1.73 mmol, 1.0 eq) were mixed together in a microwave reaction vial. The mixture was stirred neat at 160 ^oC for 1 h under microwave radiation. The crude product was purified by silica gel chromatography to give 8-bromo-2-(furan-2-yl)-*N*-(*m*-tolyl)imidazo[1,2-*a*]pyridin-3-amine (53.3 mg, 8%) as white solid: LCMS (ESI): m/z = 369.9, $[M+3H]^+$, R_t = 1.810 min; >90% (210, 254 nm); ^1H NMR (400 MHz, DMSO) δ 8.27 (s, 1H), 8.01 (d, J = 5.9 Hz, 1H),

7.76 (d, J = 1.0 Hz, 1H), 7.68 (d, J = 6.5 Hz, 1H), 7.03 (s, 1H), 6.88 (s, 1H), 6.71 (s, 1H), 6.58 (dd, J = 3.4, 1.8 Hz, 1H), 6.33 (dd, J = 8.0, 2.0 Hz, 1H), 6.09 (d, J = 2.1 Hz, 1H), 6.05 (d, J = 7.9 Hz, 1H), 3.63 (s, 3H).

8-Bromo-*N*-(2-chlorophenyl)-2-(furan-2-yl)imidazo[1,2-*a*]pyridin-3-amine (12).

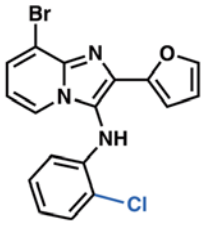

Step 1. Preparation of N-(2-chlorophenyl)formamide.

A mixture of 2-chloroaniline (3 g, 23.6 mmol, 1 eq), formic acid (30 mL), and sodium formate (1.6 g, 23 mmol, 1 eq) in a 50 mL round-bottom flask was stirred with a magnetic stir bar at room temperature. The progress of the reaction was monitored by TLC. When the reaction finished, 30 mL of EtOAc was added into the system, and the organic solvent was then washed with H_2O (3 × 50 mL) and a saturated solution of $NaHCO_3$ (50mL). After drying with Na_2SO_4, the solvent was removed under reduced pressure. The resulting residue (2 g, 56%) containing the *N*-(2-chlorophenyl)formamide was taken on to the next step without further purification: LCMS (ESI): m/z = 156.1, $[M+H]^+$, R_t = 1.330 min; >95% (210, 254 nm).

Step 2. Preparation of 1-chloro-2-isocyanobenzene.

To a solution of N-(2-chlorophenyl)formamide (3.5 g, 22.5 mmol, 1 eq) and Et_3N (7.5 g, 74.5 mmol, 3.3 eq) in anhydrous DCM (40 mL) was added dropwise $POCl_3$ (3.8 g, 24.8 mmol, 1.1 eq) at 0 ^oC under a nitrogen atmosphere over 35 min. Then the reaction mixture

was stirred at 0 ^{o}C for 1 h. After completion, the reaction mixture was poured onto a saturated solution of $NaHCO_3$ at 0 ^{o}C. The mixture was extracted by DCM. The organic phase was dried over Na_2SO_4 and the solvent was removed under reduced pressure. The crude product 1-chloro-2-isocyanobenzene was purified by silica gel column chromatography to give the product as a yellow green liquid (2.4 g, 80%). The isocyanide was used directly in step 3 without further purification.

Step 3. Preparation of 8-bromo-N-(2-chlorophenyl)-2-(furan-2-yl)imidazo[1,2-a]pyridin-3-amine.

To 1-chloro-2-isocyanobenzene (500 mg, 3.64 mmol, 1.0 eq) from step 2, furan-2-carbaldehyde (350 mg, 3.64 mmol, 1.0 eq), and 3-bromopyridin-2-amine (627 mg, 3.64 mmol, 1.0 eq) were mixed together in a microwave reaction vial. The mixture was heated neat at 160 ^{o}C for 1 h under microwave radiation. The crude product was purified by silica gel chromatography to give 8-bromo-*N*-(2-chlorophenyl)-2-(furan-2-yl)imidazo[1,2-a]pyridin-3-amine (45 mg, <5%) as white solid: LCMS (ESI): m/z = 389.8, $[M+H]^+$, R_t = 1.855 min; >95% (210, 254 nm); ^{1}H NMR (400 MHz, DMSO) δ 8.06 (d, J = 5.9 Hz, 1H), 7.98 (s, 1H), 7.74 (d, J = 1.1 Hz, 1H), 7.70 (d, J = 6.6 Hz, 1H), 7.42 (dd, J = 7.9, 1.4 Hz, 1H), 6.98 (s, 1H), 6.88 (t, J = 7.0 Hz, 1H), 6.77 (s, 1H), 6.63 (d, J = 3.3 Hz, 1H), 6.56 (dd, J = 3.3, 1.8 Hz, 1H), 6.11 (dd, J = 8.2, 1.4 Hz, 1H).

<u>8-Bromo-2-(furan-2-yl)-*N*-(3-methoxyphenyl)imidazo[1,2-*a*]pyridin-3-amine (14).</u>

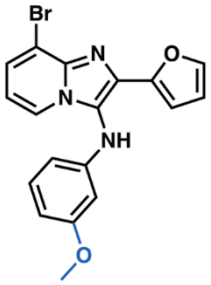

Step 1. Preparation of N-(3-methoxyphenyl)formamide.

A mixture of 3-methoxyaniline (3 g, 24.39 mmol, 1 eq), formic acid (30 mL), and sodium formate (16 g, 243.9 mmol, 10 eq) in a 50 mL round-bottom flask was stirred with a magnet at room temperature. The progress of the reaction was monitored by TLC. When the reaction finished, 30 mL of EtOAc was added into the system, and the organic solvent was then washed with H_2O (3 × 50 mL) and a saturated solution of $NaHCO_3$ (50 mL). After drying with Na_2SO_4, the solvent was removed under reduced pressure. The resulting residue (2.4 g, 15.89 mmol, 66.6 %) containing the *N*-(3-methoxyphenyl)formamide was taken on to the next step without additional purification: LCMS (ESI): m/z = 152.0, $[M+H]^+$, R_t = 0.635 min; >95% (210, 254 nm).

Step 2. Preparation of starting material 1-isocyano-3-methoxybenzene.

To a solution of *N*-(3-methoxyphenyl)formamide (2.4 g, 15.8 mmol, 1 eq) and Et_3N (5.29 g, 52.4 mmol, 3.3 eq) in anhydrous DCM (40 mL) was added dropwise $POCl_3$ (2.67 g, 17.4 mmol, 1.1 eq) at 0°C under a nitrogen atmosphere over 35 min. Then the reaction mixture was stirred at 0°C for 1 h. After completion, the reaction mixture was poured into a saturated solution of $NaHCO_3$ at 0°C. Then the mixture was extracted by DCM. The organic phase was dried over Na_2SO_4, and the solvent was removed under reduced pressure. The crude product was purified by silica gel column chromatography to give the

product as a yellow-green liquid (2.0 g, 95%). The isocyanide was used directly in step 3 without further purification.

Step 3. Preparation of 8-bromo-2-(furan-2-yl)-N-(3-methoxyphenyl)imidazo[1,2-a]pyridin-3-amine.

To a solution of 1-isocyano-3-methoxybenzene (200 mg, 1.5 mmol, 1.0 eq) from step 2 above, furan-2-carbaldehyde (144 mg,1.5 mmol, 1.0 eq), and 3-bromopyridin-2-amine (258 mg, 1.5 mmol, 1.0 eq) were combined in a microwave reaction vial. The mixture was heated neat at 160 ^{o}C for 1 h under microwave radiation with stirring. The crude product was purified by silica gel chromatography to give title compound 8-bromo-2-(furan-2-yl)-*N*-(3-methoxyphenyl)imidazo[1,2-a]pyridin-3-amine (40 mg, 7%) as a white solid: LCMS (ESI): m/z = 385.9, $[M+H+2]^+$, R_t = 1.557 min; >95% (210, 254 nm); ^{1}H NMR (400 MHz, DMSO) δ 8.27 (s, 1H), 8.01 (d, J = 5.9 Hz, 1H), 7.76 (d, J = 1.0 Hz, 1H), 7.68 (d, J = 6.5 Hz, 1H), 7.03 (s, 1H), 6.88 (s, 1H), 6.71 (s, 1H), 6.58 (dd, J = 3.4, 1.8 Hz, 1H), 6.33 (dd, J = 8.0, 2.0 Hz, 1H), 6.09 (d, J = 2.1 Hz, 1H), 6.05 (d, J = 7.9 Hz, 1H), 3.63 (s, 3H).

<u>*Tert*-butyl 3-(8-bromo-7-fluoro-3-(o-tolylamino)imidazo[1,2-*a*]pyridin-2-yl)azetidine-1-carboxylate (PBJ1).</u>

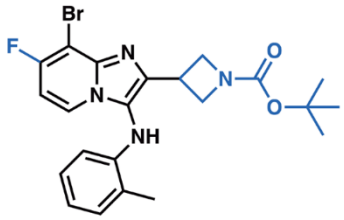

A mixture of 1-isocyano-2-methylbenzene (122.7 mg, 1.59 mmol, 1.05 eq), *tert*-butyl-3-formylazetidine-1-carboxylate (194 mg, 1.05 mmol, 1.0 eq), and 3-bromo-4-fluoropyridin-

2-amine (200 mg, 1.05 mmol, 1.0 eq) was combined in a microwave reaction vial. The mixture was stirred at 160 °C for 1 h under microwave radiation. The crude product was purified by RP-HPLC to give the title compound (102.2 mg, 6%) as yellow solid: LCMS (ESI): m/z = 477.0, $[M+3H]^+$, R_t = 1.557 min; >95% (210, 254 nm); ^{1}H NMR (400 MHz, DMSO) δ 12.5 (m, 1H), 8.19 (s, 1H), 7.72 (d, J = 6.8 Hz, 1H), 7.50 (s, 1H), 7.14 (d, J = 6.8 Hz, 1H), 6.87 (dt, J = 14.5, 7.0 Hz, 2H), 6.69 (t, J = 7.4 Hz, 1H), 5.90 (d, J = 8.0 Hz, 1H), 2.40 (s, 3H).

<u>8-(Difluoromethyl)-2-(furan-2-yl)-*N*-(*o*-tolyl)imidazo[1,2-*a*]pyridin-3-amine (PBJ2).</u>

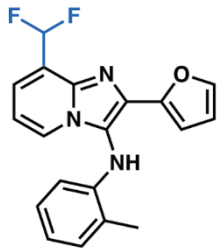

A mixture of 1-isocyano-2-methylbenzene (150 mg, 1.28 mmol), furan-2-carbaldehyde (123 mg, 1.28 mmol), and 3-(difluoromethyl)pyridin-2-amine (185 mg, 1.28 mmol) were combined in a microwave reaction vial and heated neat at 150 °C for 1 h under microwave radiation. After completion, the reaction was cooled and purified by flash chromatography (EtOAc/hexanes). The crude product containing fractions were concentrated and further purified by HPLC. The final product was isolated as a yellow solid to give 8-(difluoromethyl)-2-(furan-2-yl)-*N*-(*o*-tolyl)imidazo[1,2-*a*]pyridin-3-amine (34.79 mg, 8%): LCMS (ESI): m/z = 340.1, $[M+H]^+$, R_t = 1.35 min; >95% (210, 254 nm); ^{1}H NMR (400 MHz, DMSO) δ 8.14 (d, J = 6.6 Hz, 1H), 7.74 (s, 1H), 7.63 (s, 0.24H), 7.59 (d, J = 6.7 Hz, 1H), 7.49 (s, 1.5H), 7.36 (s, 0.26H), 7.15 (d, J = 7.3 Hz, 1H), 7.03 (t, J = 6.9 Hz, 1H), 6.84

(t, J = 7.6 Hz, 1H), 6.67 (t, J = 7.3 Hz, 1H), 6.62 (d, J = 3.2 Hz, 1H), 6.55 (dd, J = 3.3, 1.8 Hz, 1H), 5.87 (d, J = 7.9 Hz, 1H), 2.41 (s, 3H).

Figures:

FIGURE 1

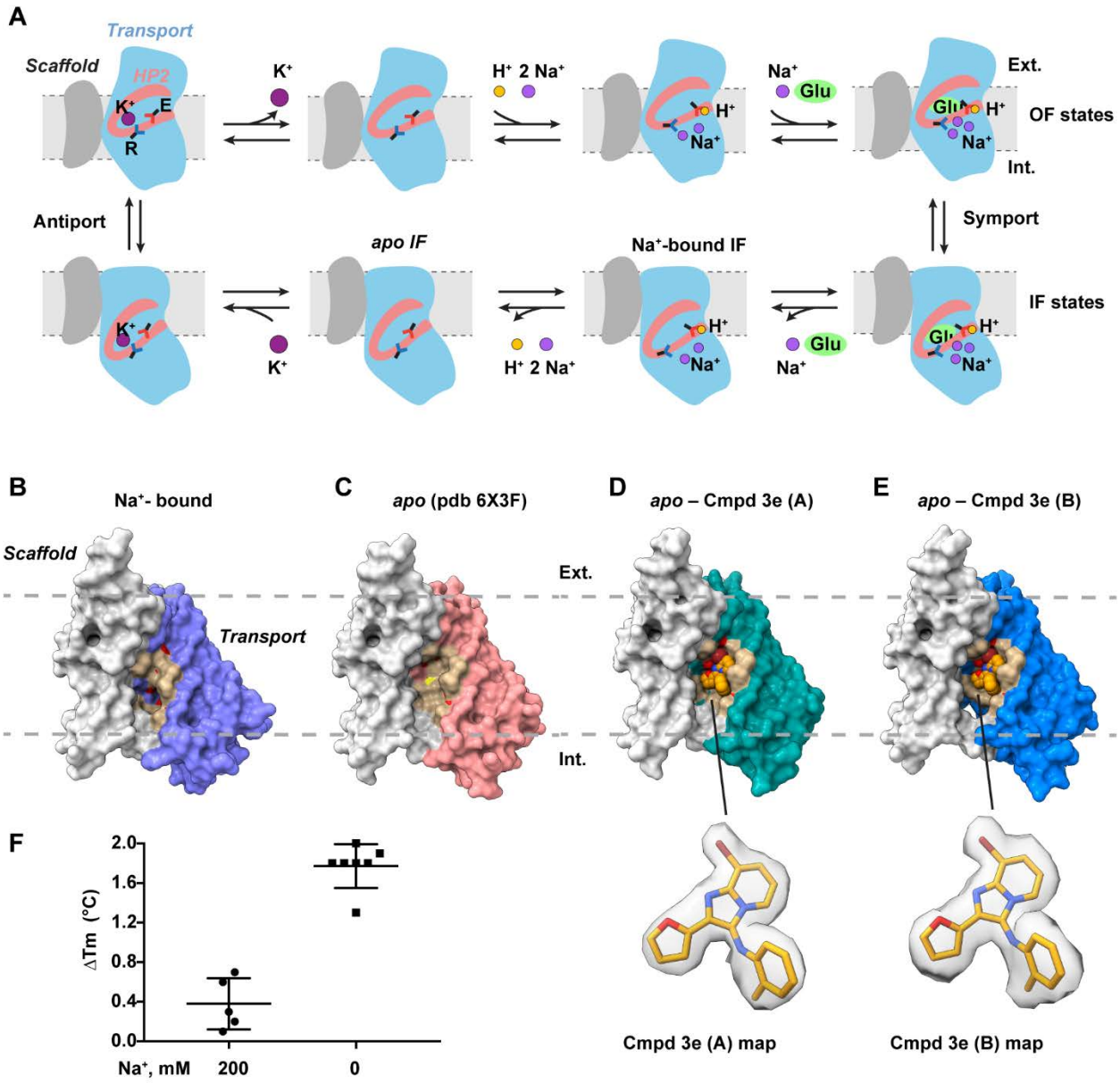

Figure 1. Compound 3e binds to *apo* inward-facing SLC1A1g protomers. (**A**) The transport cycle of SLC1A1 transporters. Outward-facing (OF) carriers bind substrate and symported ions under occluding HP2 (raspberry); the transport domain (blue) translocates relative to the stationary scaffold domain (white) into the inward-facing (IF) state, where it releases the substrate and ions; the transport domain returns into the OF state after binding a K^+ ion. Key ion and substrate-binding arginine (R) and glutamate (E) residues are shown for reference. (**B, C**) The surface representation of structures of Na^+-bound SLC1A1g observed in the cryo-EM sample **(B**) and the *apo* transporter (**C**, PDB access code 6X3F) in IF. The structures show an enlarged drug-binding pocket in the *apo* carrier. The scaffold domain is colored white, the transport domain is in various colors, and the residues within 4 Å of **3e** in the drug-bound states are colored in tan. The dotted gray lines represent the approximate boundaries of the membrane bilayer. (**D, E**). Structures of SLC1A1g bound to **3e** as seen in the structural classes A (**D**) and B (**E**). The compound **3e** is shown as spheres and colored orange. The EM density contoured at 5σ around the modeled **3e** is shown below the panels. (**F**) Thermal stabilization of SLC1A1g by 100 µM **3e** in the presence and absence of 200 mM Na^+.

FIGURE 2

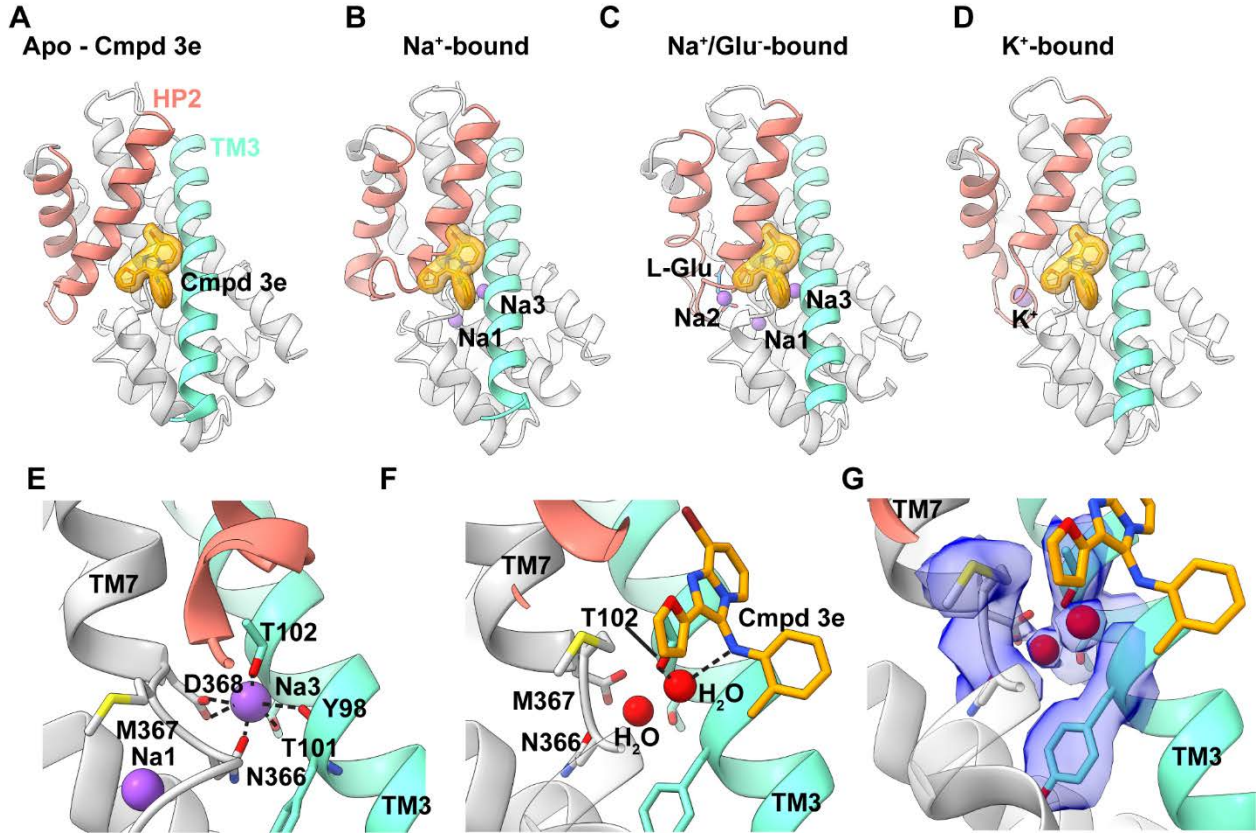

880

881

882

Figure 2. Compound 3e and Na^+ ions compete for binding to SLC1A1g. (**A-D**) Structures of the *apo* SLC1A1g transport domain bound to **3e** (**A**). Modeled **3e** bound to SLC1A1g with Na^+ only (**B**), Na^+ and L-Glu (**C**), and with K^+ (**D**). The transport domain is depicted as a gray cartoon, with HP2 and TM3 highlighted in raspberry and green-cyan, respectively. L-Glu is depicted in blue, and Na^+ and the K^+ ions in purple. **3e** is shown as an orange surface where it is observed in cryo-EM (**C**) or modeled at corresponding positions (**B-D**). Modeling shows that in Na^+-bound transporter, with or without Glu, the compound would sterically clash with HP2. The binding pocket is preserved in the K^+-bound transporter. (**E, F**) Close-up view of the Na3 and **3e** binding sites in Na^+- and **3e**-bound states of SLC1A1g, respectively. Residues coordinating Na3 are shown as sticks. T102 coordinates Na3 (**E**) and, via a water-mediated hydrogen bond, **3e** (**F**). (**G**) An EM density map contoured at 5σ around the modeled side chains and waters in **3e-**bound SLC1A1g in the B structural class.

FIGURE 3

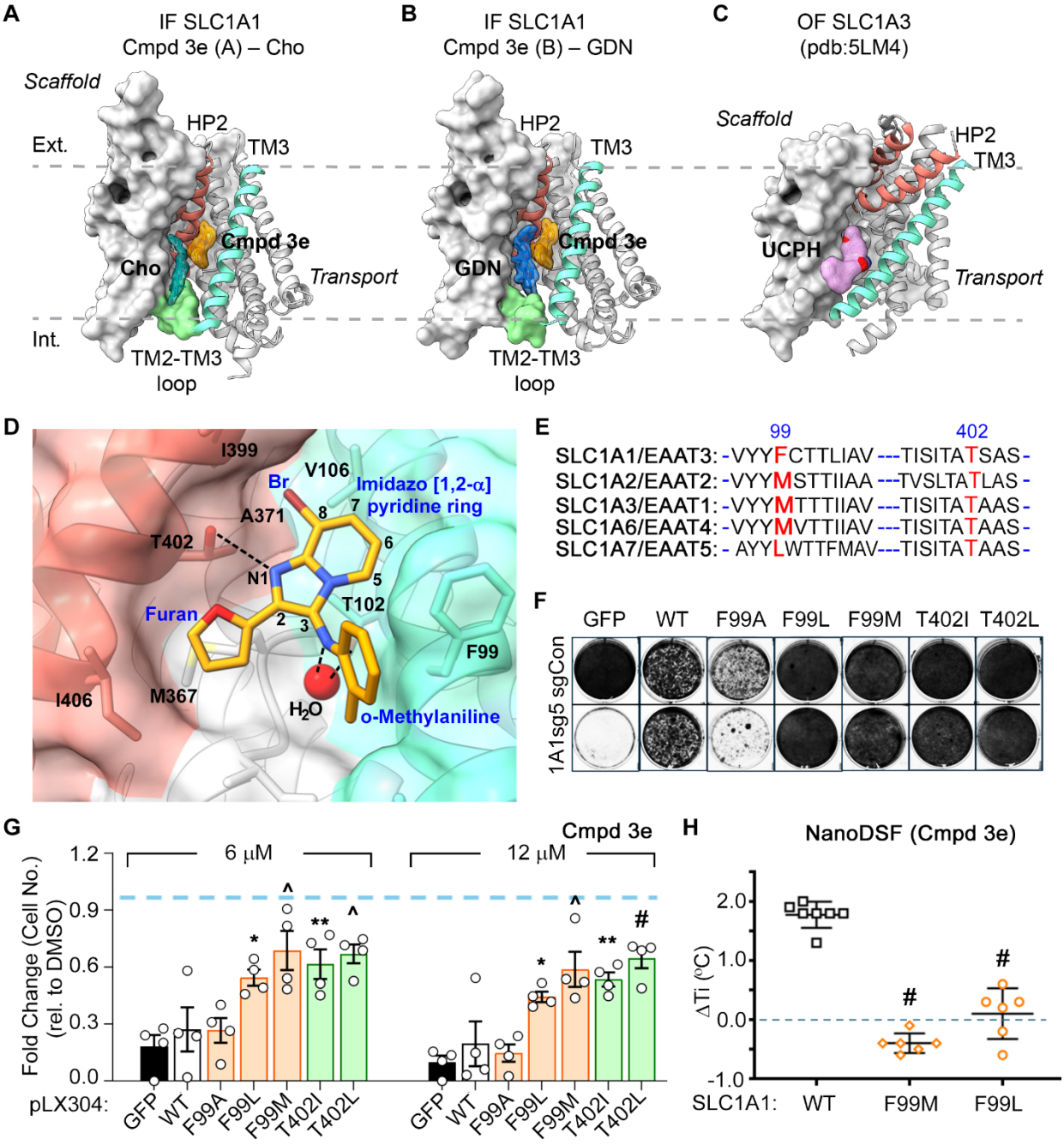
A
IF SLC1A1
Cmpd 3e (A) – Cho
Scaffold
Ext.
HP2
TM3
Cmpd 3e
Cho
Transport
Int.
TM2-TM3
loop
B
IF SLC1A1
Cmpd 3e (B) – GDN
HP2
TM3
Cmpd 3e
GDN
TM2-TM3
loop
C
OF SLC1A3
(pdb:5LM4)
Scaffold
HP2
TM3
UCPH
Transport
D
I399
V106
Br
Imidazo [1,2-α]
pyridine ring
A371
T402
N1
T102
Furan
F99
I406
M367
H2O
o-Methylaniline
E
99
402
SLC1A1/EAAT3: -VYYFCTTLIAV---TISITATSAS-
SLC1A2/EAAT2: -VYYMSTTIIAA---TVSLTATLAS-
SLC1A3/EAAT1: -VYYMTTTIIAV---TISITATAAS-
SLC1A6/EAAT4: -VYYMVTTIIAV---TISITATAAS-
SLC1A7/EAAT5: - AYYLWTTFMAV---TISITATAAS-
F
GFP
WT
F99A
F99L
F99M
T402I
T402L
1A1sg5 sgCon
G
Cmpd 3e
6 μM
12 μM
Fold Change (Cell No.)
(rel. to DMSO)
pLX304:
GFP
WT
F99A
F99L
F99M
T402I
T402L
H
NanoDSF (Cmpd 3e)
ΔTi (°C)
SLC1A1:
WT
F99M
F99L

Figure 3. Binding selectivity determinants and SLC1A1 drug-resistant mutants. (**A, B**) Structures of SLC1A1g bound to **3e** with cholesterol in structural class A (Cho, **A**) and GDN in class B (**B**) sandwiched between the drug and the scaffold domain. Scaffold and transport domains are shown in surface and cartoon representations, respectively. The color scheme is as in Figure 2, with the TM2-TM3 loop colored light green. The EM density around **3e**, cholesterol, and GDN is contoured at 5σ and colored orange, teal, and slate blue, respectively. (**C**) Structure of SLC1A3/EAAT1 in OF state bound to UCPH-101 (PDB code 5LM4). The drug is colored pink and shown in surface representation. Note that UCPH-101 is more inwardly positioned than **3e** and coordinated by the cytoplasmic end of TM3. (**D**) A close-up view of the **3e** binding pocket in cartoon and transparent surface representation. The SLC1A1 residues within 4 Å are shown as sticks and labeled in black. The **3e** backbone is numbered, and key functional groups are labeled in blue. Hydrogen bonds with the resolved water molecule (red) are shown as dashed lines. (**E**) Sequence alignment around TM3 residue F99 and HP2 residue T402 for SLC1 proteins. T402 is conserved while F99 is variable (**F**) Crystal violet staining of A498 cells that were lentivirally transduced to express sgRNA (sg5)-resistant versions of either wild-type (WT) or mutant SLC1A1, or GFP (as a control), and then transduced with sgRNA constructs to inactivate SLC1A1 (1A1sg5) or a non-targeting control (sgCon). (**G**) Viable cell number of isogenic A498 cells expressing the indicated forms of SLC1A1 (or GFP control) and then cultured in the presence of the indicated concentrations of **3e** for 20 days. Cell numbers, relative to vehicle DMSO treatment (blue dashed line), were represented as mean ± S.D. and compared to the GFP arm using one-way ANOVA with Dunnett's multiple comparison test. *$p<0.05$, **$p<0.01$, ^$p<0.001$, #$p<0.0001$. (**E**) NanoDSF results showing

changes in *Ti* for WT SLC1A1g versus the F99L and F99M mutants that lose the ability to bind **3e**. Experiments were repeated using two independent protein preparations with at least three technical repeats each. #$p<0.0001$.

FIGURE 4

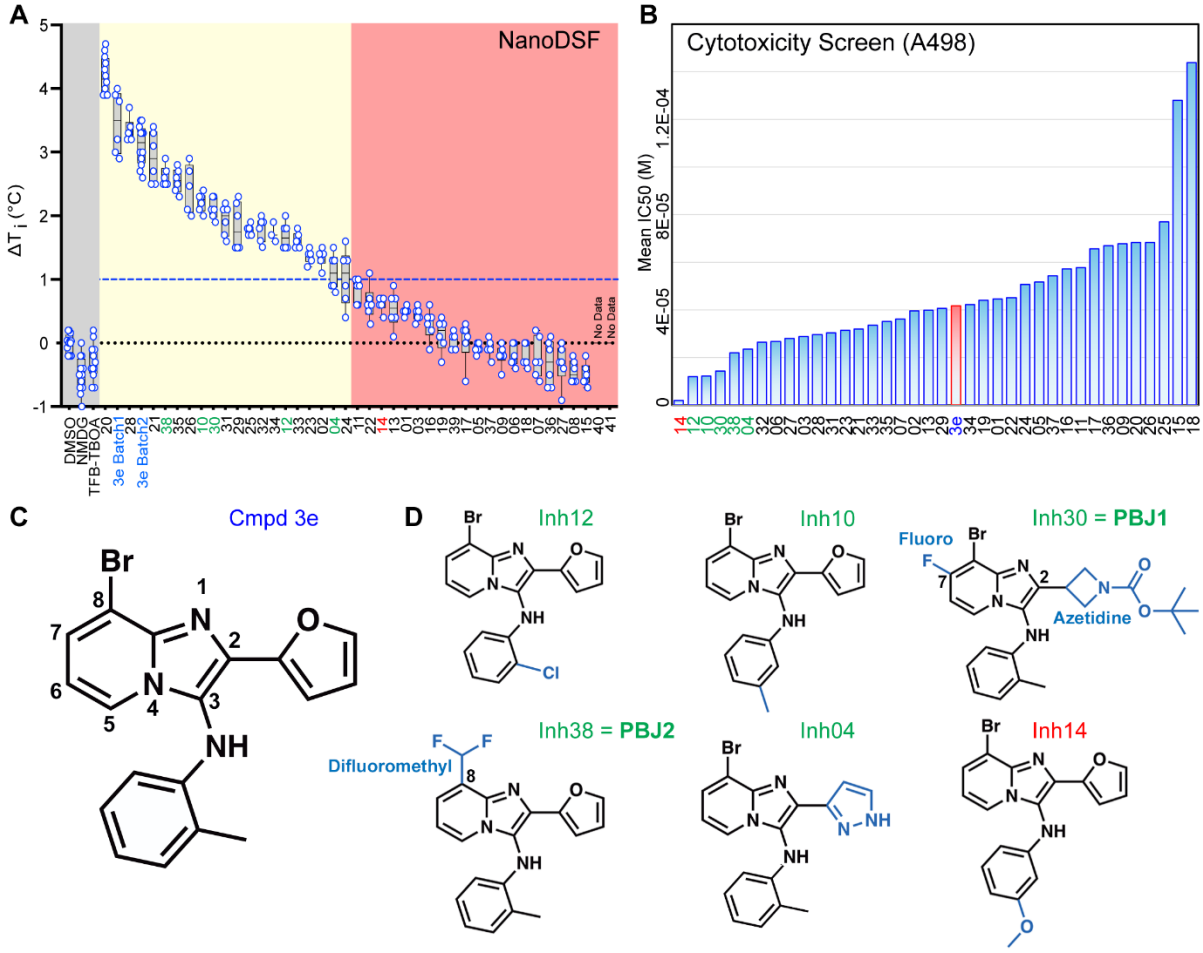
A
NanoDSF
ΔT i (°C)
DMSO
NMDG
TFB-TBOA
3e Batch1
3e Batch2
No Data
B
Cytotoxicity Screen (A498)
Mean IC50 (M)
C
Cmpd 3e
Br
NH
D
Inh12
Inh10
Inh30 = PBJ1
Fluoro
Azetidine
Inh38 = PBJ2
Difluoromethyl
Inh04
Inh14

Figure 4. Screening identifies novel BIA inhibitors. (**A**) Screening of **3e** analogs in thermal shift NanoDSF assays. Gray, yellow, and salmon regions represent, respectively, controls, compounds that stabilize SLC1A1g by more than 1°C, suggesting binding, and compounds that do not significantly stabilize SLC1A1g, suggesting they do not bind. No data were obtained for compounds interfering with fluorescence measurements (e.g., **40** and **41**). Results are averages of at least two independent biological repeats, each comprising at least three technical repeats. Standard errors are shown. (**B**) Screening of **3e** analogs in high-throughput cytotoxicity assay using kidney cancer A498 cells. Mean IC_{50} values from two independent experiments are shown as blue columns and compared to **3e** control (red column). Selected compounds are colored green. (**C, D**) Chemical structure of the parental **3e** (**C**) and selected BIA compounds (**D**). Inhibitor **14** (red) is a highly cytotoxic off-target compound.

FIGURE 5

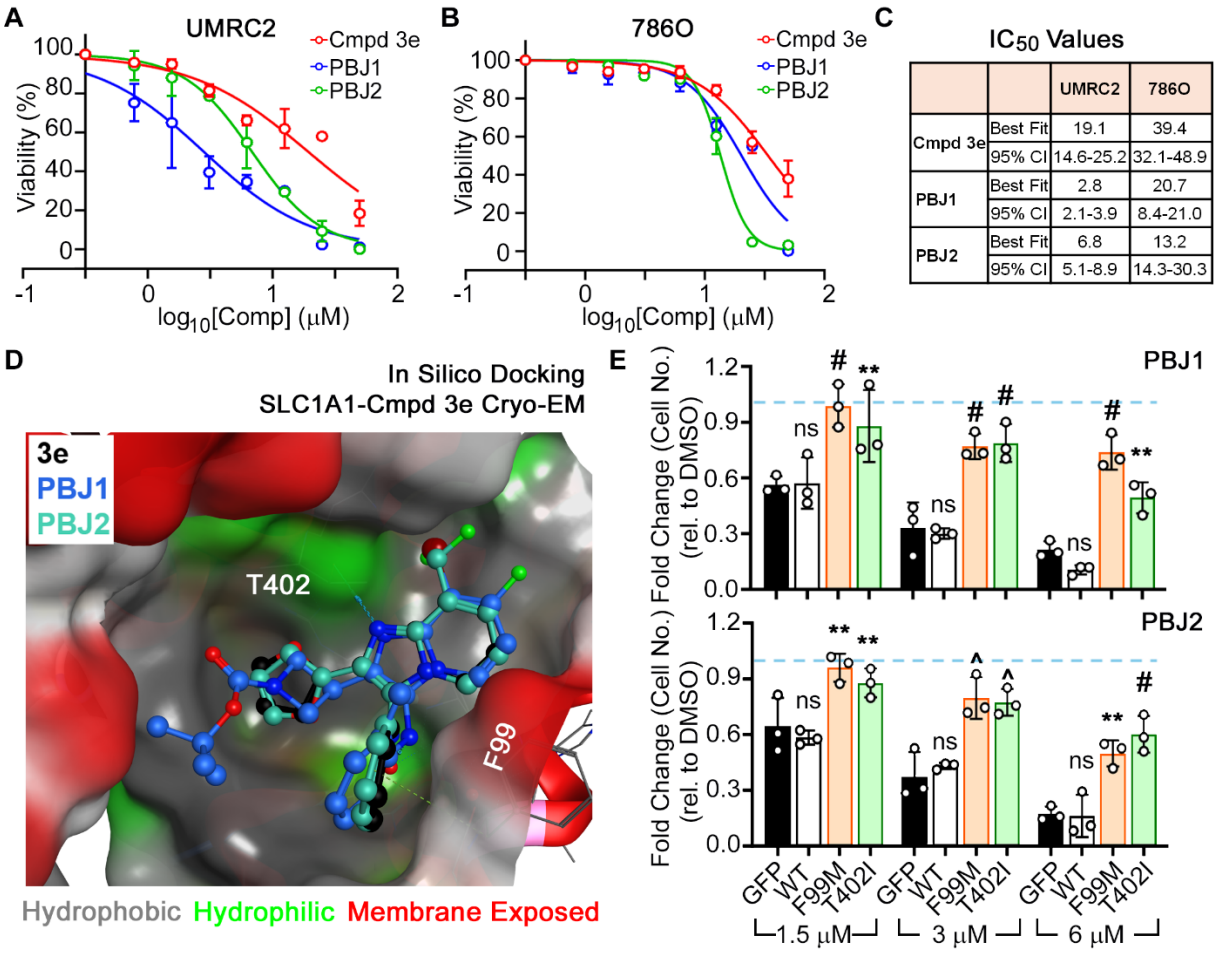

		UMRC2	786O
Cmpd 3e	Best Fit	19.1	39.4
	95% CI	14.6-25.2	32.1-48.9
PBJ1	Best Fit	2.8	20.7
	95% CI	2.1-3.9	8.4-21.0
PBJ2	Best Fit	6.8	13.2
	95% CI	5.1-8.9	14.3-30.3

Figure 5. The antiproliferative properties of novel BIA compounds are on-target. (**A**-**C**) Dose-dependent cytotoxic effects of the parental **3e** and the novel PBJ1 and PBJ2 molecules on UMRC2 (**A**) and 786O (**B**) kidney cancer cells with fitted IC_{50} values (**C**). (**D**) PBJ1 and PBJ2 docked into the **3e** binding site. (**E**) Fold change in cell number, relative to vehicle DMSO treatment (blue dashed line), in A498 cells that were lentivirally transduced to expressing the indicated WT or drug-resistant mutants of SLC1A1 mutants, or GFP control, and then cultured in the presence of the indicated concentrations of PBJ1 or PBJ2 for 14-20 days. Data normalized to the DMSO arm was plotted as mean ± S.D. and statistically compared to the GFP arm by one-way ANOVA adjusted using Dunnett's multiple comparison test. **$p<0.01$, #$p<0.0001$, and n.s. = not significant.

FIGURE 6

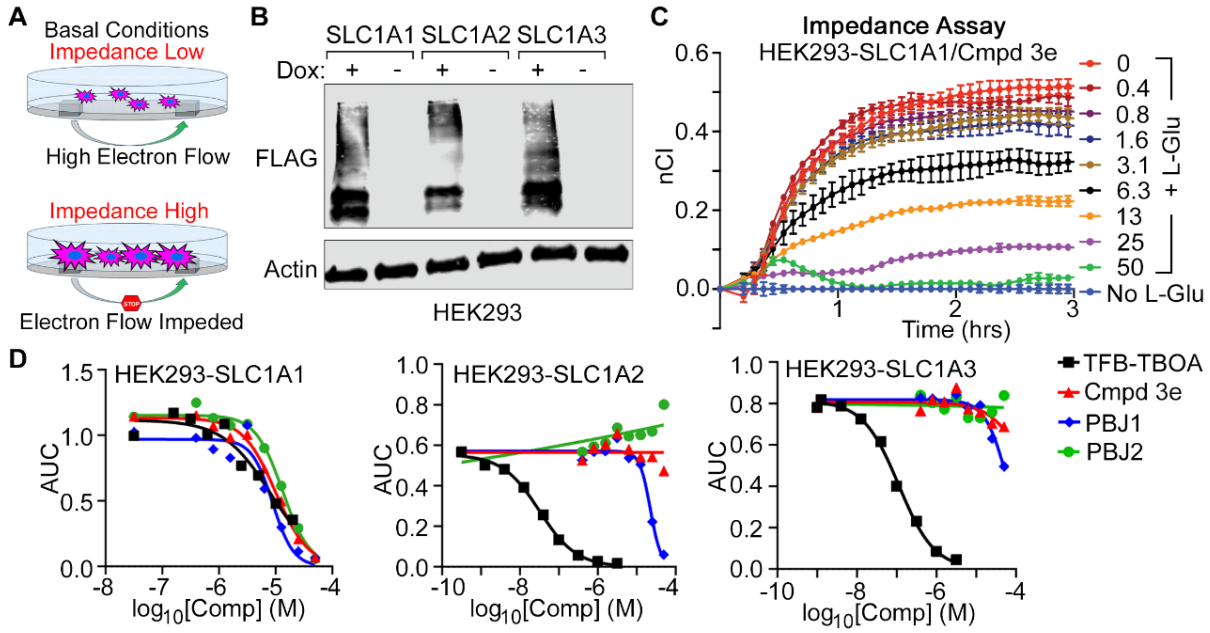

954

955

Figure 6. Novel antiproliferative BIA compounds inhibit transport by SLC1A1. (**A**) Experimental design of the impedance assay. (**B**) Western blot showing SLC1 expression in HEK293 cells stably transfected with FLAG-tagged Dox-inducible versions of human *SLC1A1*, *SLC1A2*, and *SLC1A3* genes. (**C**) Time-dependent impedance increases in HEK293 cells expressing SLC1A1 in the presence of 1 mM L-Glu and increasing concentrations of **3e**. (**D**) Dose-dependent inhibition of impedance as measured by changes in integrated Area Under the Curve (AUC) upon treatment of cells in (**B**) and (**C**) with the indicated BIA compounds or **3e** and TFB-TBOA as controls.

FIGURE 7

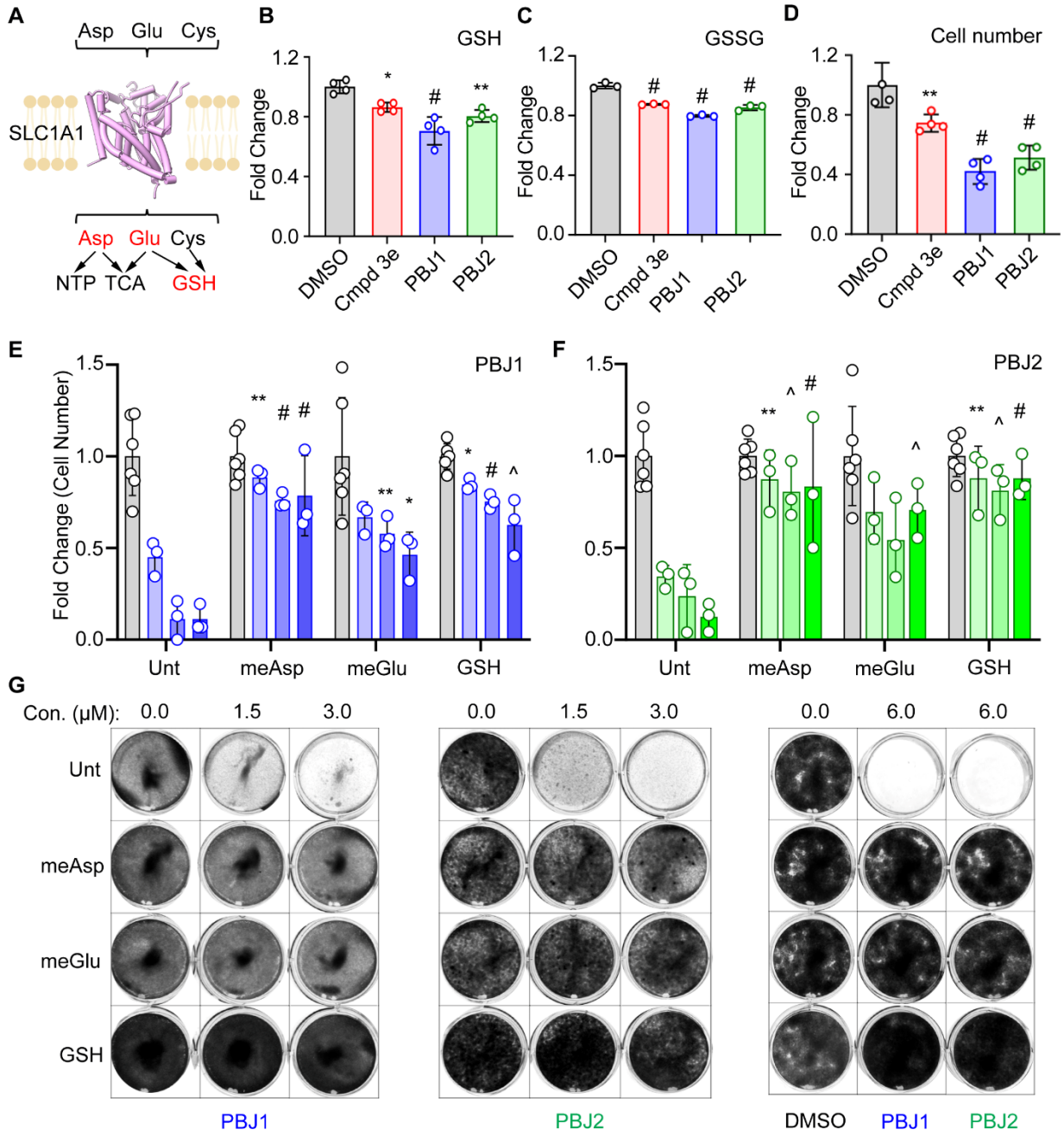
A
Asp Glu Cys
SLC1A1
Asp Glu Cys
NTP TCA GSH
B
GSH
Fold Change
DMSO
Cmpd 3e
PBJ1
PBJ2
C
GSSG
D
Cell number
E
PBJ1
Fold Change (Cell Number)
Unt
meAsp
meGlu
GSH
F
PBJ2
G
Con. (μM): 0.0 1.5 3.0 0.0 1.5 3.0 0.0 6.0 6.0
Unt
meAsp
meGlu
GSH
PBJ1
PBJ2
DMSO PBJ1 PBJ2

Figure 7. BIA compounds cause metabolic vulnerabilities in cancer cells. (**A**) SLC1A1 uptakes Asp, Glu, and Cys amino acids, which are necessary for the synthesis of nucleotides (NTPs), enter the TCA cycle, and are precursors of glutathione (GSH) biosynthesis. (**B**-**D**) Intracellular levels of reduced glutathione (GSH) (**B**) or oxidized glutathione (GSSG) (**C**), and changes in cell number (**D**), in A498 cells that were treated with 5 μM of the indicated compounds, or DMSO control. Data plotted as mean ± S.D. was statistically compared to the DMSO arm by ANOVA adjusted using Dunnett's multiple comparison test. (**E**-**G**) Cell counts measured using ViCell upon treatment with PBJ1 (**E**) or PBJ2 (**F**), and representative plates stained using crystal violet (**G**), in A498 cells that were grown in the presence of the indicated concentrations of PBJ1 or PBJ2, along with no treatment (Unt), 100 μM membrane-permeable methyl esters of L-Asp and L-Glu (meAsp, meGlu), or 1 mM GSH, as indicated, for 14-20 days. In (**B**) to (**F**), *$p<0.05$, **$p<0.01$, ^$p<0.001$, and #$p<0.0001$.

REFERENCES

1. Hediger, M.A., Clemencon, B., Burrier, R.E. & Bruford, E.A. The ABCs of membrane transporters in health and disease (SLC series): introduction. *Mol Aspects Med* **34**, 95-107 (2013).
2. Lin, L., Yee, S.W., Kim, R.B. & Giacomini, K.M. SLC transporters as therapeutic targets: emerging opportunities. *Nat Rev Drug Discov* **14**, 543-60 (2015).
3. Grubb, T. *et al.* The SLC1A1/EAAT3 Dicarboxylic Amino Acid Transporter is an Epigenetically Dysregulated Nutrient Carrier that Sustains Oncogenic Metabolic Programs. *bioRxiv*, 2023.09.04.556240 (2023).
4. Kaelin, W.G. Von Hippel-Lindau disease. *Annu Rev Pathol* **2**, 145-73 (2007).
5. Yang, Z. *et al.* HIF-1alpha drives resistance to ferroptosis in solid tumors by promoting lactate production and activating SLC1A1. *Cell Rep* **42**, 112945 (2023).
6. Guo, W. *et al.* Dysregulated Glutamate Transporter SLC1A1 Propels Cystine Uptake via Xc(-) for Glutathione Synthesis in Lung Cancer. *Cancer Res* **81**, 552-566 (2021).
7. Wen, D. *et al.* NF-kappaB-mediated EAAT3 upregulation in antioxidant defense and ferroptosis sensitivity in lung cancer. *Cell Death Dis* **16**, 124 (2025).
8. Xiong, J. *et al.* SLC1A1 mediated glutamine addiction and contributed to natural killer T-cell lymphoma progression with immunotherapeutic potential. *EBioMedicine* **72**, 103614 (2021).
9. Palos, T.P., Ramachandran, B., Boado, R. & Howard, B.D. Rat C6 and human astrocytic tumor cells express a neuronal type of glutamate transporter. *Brain Res Mol Brain Res* **37**, 297-303 (1996).

10. Bailey, C.G. *et al.* Loss-of-function mutations in the glutamate transporter SLC1A1 cause human dicarboxylic aminoaciduria. *J Clin Invest* **121**, 446-53 (2011).

11. Watts, S.D., Torres-Salazar, D., Divito, C.B. & Amara, S.G. Cysteine transport through excitatory amino acid transporter 3 (EAAT3). *PLoS One* **9**, e109245 (2014).

12. Kanai, Y. & Hediger, M.A. Primary structure and functional characterization of a high-affinity glutamate transporter. *Nature* **360**, 467-71 (1992).

13. Zerangue, N. & Kavanaugh, M.P. Flux coupling in a neuronal glutamate transporter. *Nature* **383**, 634-7 (1996).

14. Himi, T., Ikeda, M., Yasuhara, T., Nishida, M. & Morita, I. Role of neuronal glutamate transporter in the cysteine uptake and intracellular glutathione levels in cultured cortical neurons. *J Neural Transm (Vienna)* **110**, 1337-48 (2003).

15. Sullivan, L.B. *et al.* Supporting Aspartate Biosynthesis Is an Essential Function of Respiration in Proliferating Cells. *Cell* **162**, 552-63 (2015).

16. Garcia-Bermudez, J. *et al.* Aspartate is a limiting metabolite for cancer cell proliferation under hypoxia and in tumours. *Nat Cell Biol* **20**, 775-781 (2018).

17. Birsoy, K. *et al.* An Essential Role of the Mitochondrial Electron Transport Chain in Cell Proliferation Is to Enable Aspartate Synthesis. *Cell* **162**, 540-51 (2015).

18. Gameiro, P.A. *et al.* In vivo HIF-mediated reductive carboxylation is regulated by citrate levels and sensitizes VHL-deficient cells to glutamine deprivation. *Cell Metab* **17**, 372-85 (2013).

19. Ling, Z.N. *et al.* Amino acid metabolism in health and disease. *Signal Transduct Target Ther* **8**, 345 (2023).

20. Chen, J., Cui, L., Lu, S. & Xu, S. Amino acid metabolism in tumor biology and therapy. *Cell Death Dis* **15**, 42 (2024).

21. Danbolt, N.C., Storm-Mathisen, J. & Kanner, B.I. An [Na+ + K+]coupled L-glutamate transporter purified from rat brain is located in glial cell processes. *Neuroscience* **51**, 295-310 (1992).

22. Danbolt, N.C., Furness, D.N. & Zhou, Y. Neuronal vs glial glutamate uptake: Resolving the conundrum. *Neurochem Int* **98**, 29-45 (2016).

23. Peghini, P., Janzen, J. & Stoffel, W. Glutamate transporter EAAC-1-deficient mice develop dicarboxylic aminoaciduria and behavioral abnormalities but no neurodegeneration. *EMBO J* **16**, 3822-32 (1997).

24. Aoyama, K., Matsumura, N., Watabe, M. & Nakaki, T. Oxidative stress on EAAC1 is involved in MPTP-induced glutathione depletion and motor dysfunction. *Eur J Neurosci* **27**, 20-30 (2008).

25. Aoyama, K. *et al.* Neuronal glutathione deficiency and age-dependent neurodegeneration in the EAAC1 deficient mouse. *Nat Neurosci* **9**, 119-26 (2006).

26. Canul-Tec, J.C. *et al.* Structure and allosteric inhibition of excitatory amino acid transporter 1. *Nature* **544**, 446-451 (2017).

27. Canul-Tec, J.C. *et al.* The ion-coupling mechanism of human excitatory amino acid transporters. *EMBO J* **41**, e108341 (2022).

28. Kato, T. *et al.* Structural insights into inhibitory mechanism of human excitatory amino acid transporter EAAT2. *Nat Commun* **13**, 4714 (2022).

29. Qiu, B. & Boudker, O. Symport and antiport mechanisms of human glutamate transporters. *Nat Commun* **14**, 2579 (2023).

30. Qiu, B. & Boudker, O. Structural basis of excitatory amino acid transporter 3 substrate recognition. *Proc Natl Acad Sci U S A* **122**, e2501627122 (2025).

31. Qiu, B., Matthies, D., Fortea, E., Yu, Z. & Boudker, O. Cryo-EM structures of excitatory amino acid transporter 3 visualize coupled substrate, sodium, and proton binding and transport. *Sci Adv* **7**(2021).

32. Reyes, N., Ginter, C. & Boudker, O. Transport mechanism of a bacterial homologue of glutamate transporters. *Nature* **462**, 880-5 (2009).

33. Shimamoto, K. *et al.* DL-threo-beta-benzyloxyaspartate, a potent blocker of excitatory amino acid transporters. *Mol Pharmacol* **53**, 195-201 (1998).

34. Shimamoto, K. *et al.* Characterization of novel L-threo-beta-benzyloxyaspartate derivatives, potent blockers of the glutamate transporters. *Mol Pharmacol* **65**, 1008-15 (2004).

35. Wu, P., Bjorn-Yoshimoto, W.E., Staudt, M., Jensen, A.A. & Bunch, L. Identification and Structure-Activity Relationship Study of Imidazo[1,2-a]pyridine-3-amines as First Selective Inhibitors of Excitatory Amino Acid Transporter Subtype 3 (EAAT3). *ACS Chem Neurosci* **10**, 4414-4429 (2019).

36. Grewer, C. *et al.* Individual subunits of the glutamate transporter EAAC1 homotrimer function independently of each other. *Biochemistry* **44**, 11913-23 (2005).

37. Leary, G.P., Stone, E.F., Holley, D.C. & Kavanaugh, M.P. The glutamate and chloride permeation pathways are colocalized in individual neuronal glutamate transporter subunits. *J Neurosci* **27**, 2938-42 (2007).

38. Koch, H.P., Brown, R.L. & Larsson, H.P. The glutamate-activated anion conductance in excitatory amino acid transporters is gated independently by the individual subunits. *J Neurosci* **27**, 2943-7 (2007).

39. Boudker, O., Ryan, R.M., Yernool, D., Shimamoto, K. & Gouaux, E. Coupling substrate and ion binding to extracellular gate of a sodium-dependent aspartate transporter. *Nature* **445**, 387-93 (2007).

40. Focke, P.J., Moenne-Loccoz, P. & Larsson, H.P. Opposite movement of the external gate of a glutamate transporter homolog upon binding cotransported sodium compared with substrate. *J Neurosci* **31**, 6255-62 (2011).

41. Verdon, G., Oh, S., Serio, R.N. & Boudker, O. Coupled ion binding and structural transitions along the transport cycle of glutamate transporters. *Elife* **3**, e02283 (2014).

42. Alleva, C. *et al.* Na(+)-dependent gate dynamics and electrostatic attraction ensure substrate coupling in glutamate transporters. *Sci Adv* **6**(2020).

43. Riederer, E.A., Moenne-Loccoz, P. & Valiyaveetil, F.I. Distinct roles of the Na(+) binding sites in the allosteric coupling mechanism of the glutamate transporter homolog, Glt(Ph). *Proc Natl Acad Sci U S A* **119**, e2121653119 (2022).

44. Abrahamsen, B. *et al.* Allosteric modulation of an excitatory amino acid transporter: the subtype-selective inhibitor UCPH-101 exerts sustained inhibition of EAAT1 through an intramonomeric site in the trimerization domain. *J Neurosci* **33**, 1068-87 (2013).

45. Erichsen, M.N. *et al.* Structure-activity relationship study of first selective inhibitor of excitatory amino acid transporter subtype 1: 2-Amino-4-(4-methoxyphenyl)-7-

(naphthalen-1-yl)-5-oxo-5,6,7,8-tetrahydro-4H-chromene-3-carbonitrile (UCPH-101). *J Med Chem* **53**, 7180-91 (2010).

46. Sijben, H.J. *et al.* Impedance-Based Phenotypic Readout of Transporter Function: A Case for Glutamate Transporters. *Front Pharmacol* **13**, 872335 (2022).

47. Danbolt, N.C. Glutamate uptake. *Prog Neurobiol* **65**, 1-105 (2001).

48. Kanai, Y. *et al.* The SLC1 high-affinity glutamate and neutral amino acid transporter family. *Mol Aspects Med* **34**, 108-20 (2013).

49. Vandenberg, R.J. & Ryan, R.M. Mechanisms of glutamate transport. *Physiol Rev* **93**, 1621-57 (2013).

50. Grewer, C., Gameiro, A. & Rauen, T. SLC1 glutamate transporters. *Pflugers Arch* **466**, 3-24 (2014).

51. Zhang, Z. *et al.* Structural basis of ligand binding modes of human EAAT2. *Nat Commun* **13**, 3329 (2022).

52. Suloway, C. *et al.* Automated molecular microscopy: the new Leginon system. *J Struct Biol* **151**, 41-60 (2005).

53. Scheres, S.H. RELION: implementation of a Bayesian approach to cryo-EM structure determination. *J Struct Biol* **180**, 519-30 (2012).

54. Punjani, A., Rubinstein, J.L., Fleet, D.J. & Brubaker, M.A. cryoSPARC: algorithms for rapid unsupervised cryo-EM structure determination. *Nat Methods* **14**, 290-296 (2017).

55. Goddard, T.D. *et al.* UCSF ChimeraX: Meeting modern challenges in visualization and analysis. *Protein Sci* **27**, 14-25 (2018).

56. Emsley, P., Lohkamp, B., Scott, W.G. & Cowtan, K. Features and development of Coot. *Acta Crystallogr D Biol Crystallogr* **66**, 486-501 (2010).

57. Adams, P.D. *et al.* PHENIX: a comprehensive Python-based system for macromolecular structure solution. *Acta Crystallogr D Biol Crystallogr* **66**, 213-21 (2010).